11-1-2022

Gas hydrate characterization in sediments via x-ray microcomputed tomography

Ghazanfer Raza Abbasi
Edith Cowan University, g.abbasi@ecu.edu.au

Muhammad Arif

Abubakar Isah

Muhammad Ali
Edith Cowan University, m.ali@ecu.edu.au

Mohamed Mahmoud

See next page for additional authors

Authors

Ghazanfer Raza Abbasi, Muhammad Arif, Abubakar Isah, Muhammad Ali, Mohamed Mahmoud, Hussein Hoteit, Alireza Keshavarz, and Stefan Iglauer

Gas hydrate characterization in sediments via x-ray microcomputed tomography

Ghazanfer Raza Abbasi [a,b,c,d,*], Muhammad Arif [e], Abubakar Isah [f], Muhammad Ali [a,d,**], Mohamed Mahmoud [f], Hussein Hoteit [d], Alireza Keshavarz [a,b], Stefan Iglauer [a,b]

[a] Petroleum Engineering Discipline, Edith Cowan University, 270 Joondalup Drive Joondalup 6027, Western Australia, Australia
[b] Centre for Sustainable Energy and Resources, Edith Cowan University, 270 Joondalup Drive Joondalup 6027, Western Australia, Australia
[c] Department of Petroleum & Gas Engineering, Dawood University of Engineering and Technology, New M. A. Jinnah Rd, Jamshed Quarters Muslimabad, Karachi, Karachi City, Sindh 74800, Pakistan
[d] Physical Science & Engineering Division, King Abdullah University of Science and Technology, Thuwal, Saudi Arabia
[e] Department of Petroleum Engineering, Khalifa University, Abu Dhabi 127788, United Arab Emirates
[f] College of Petroleum Engineering and Geosciences, King Fahd University of Petroleum & Minerals, Dhahran, Saudi Arabia

ARTICLE INFO

ABSTRACT

Natural gas hydrates (NGHs) are efficient and promising energy resources because of their high energy density. In addition, NGH occurs in sediments under certain pressure and temperature conditions and has the potential to meet the increasing global energy demand. However, efficient exploitation of NGH requires a precise characterization and understanding of the hydrate formation, accumulation, and dissociation mechanisms. In this context, the microstructural characterization of gas hydrate is essential and requires specialized methods and equipment. While traditional imaging and characterization tools offer fundamental microstructural analysis, x-ray microcomputed tomography (μCT) has gained recent attention in producing high-resolution three-dimensional images of the pore structure and habits of hydrate-bearing sediments and providing the spatial distribution and morphology of gas hydrate. Further, μCT offers the direct visualization of the hydrate structure and growth habits at a high resolution ranging from the macro- to micro-metric scale; therefore, it is extensively used in NGH characterization. This review summarizes the theoretical basis of μCT imaging spanning the setup of the experimental apparatus and visualization techniques. The applications of μCT in NGH reservoir characterization, such as hydrate types and their constituents, physical and chemical properties, occurrence, and accumulation, are presented. Hydrate characterization using μCT imaging is explicitly discussed, including a general understanding of hydrate pore-habit prediction, saturation and percolation behavior, seepage and permeability, and the influence of hydrate saturation on the mechanical properties of hydrate-bearing sediments. Last, conclusions and recommendations for future research are provided. This review offers a reference for understanding the application of μCT to evaluate gas hydrates, which contributes to exploiting these energy resources.

1. Introduction

The world is moving towards the clean energy and advanced methods to meet the net zero emission targets (Al-Anssari et al., 2021; Ali, 2018; Ali et al., 2022b,a; Iglauer et al., 2022; Mahesar et al., 2020; Pal et al., 2022). Natural gas hydrates (NGHs) are the most efficient natural gas resources and have remained stable since their discovery in the 1960s. These ice-like solid compounds comprising hydrocarbons are available in marine and permafrost (permanently frozen ground)

conditions. In addition, NGHs are found in permafrost regions at depths of 0 to 900 m and marine areas at depths of 300 to 500 m (Chibura et al., 2022). Gas hydrate resources have a geographically heterogeneous distribution and exist in a far greater amount than both conventional and unconventional hydrocarbon resources, which is significant for energy provision worldwide.

Numerous aspects of gas hydrates, including hydrate formation, recovery, gas production, depressurization, reserve evaluation, and thermal gas generation, have recently been the focus of laboratory and field research (Ripmeester, 2000). Therefore, a comprehensive

---

* Corresponding author at: Petroleum Engineering Discipline, Edith Cowan University, 270 Joondalup Drive Joondalup 6027, Western Australia, Australia.
** Corresponding author at: Physical Science & Engineering Division, King Abdullah University of Science and Technology, Thuwal, Saudi Arabia.
E-mail addresses: g.abbasi@ecu.edu.au (G.R. Abbasi), muhammad.ali.2@kaust.edu.sa (M. Ali).

understanding of the physical and chemical changes during hydrate formation and decomposition is vital for refining existing gas production models from gas hydrate accumulation and for efficient recovery planning (Swinkels and Drenth, 2000). Heat capacity and thermal conductivity are critical physical properties that govern the thermal gas generation potential, whereas relative permeability characteristics depict the associated fluid flow dynamics in hydrate-bearing sediments (HBSs).

The occurrence of gas hydrate in porous media significantly depends on specific environmental conditions (temperature and pressure; (Abbasi et al., 2021a; Abbasi et al., 2021b; Chong et al., 2016; Yin et al., 2016). Further, NGHs are formed under low-temperature and high-pressure conditions where they are thermodynamically stable. This fact implies that hydrates become more stable with decreasing temperature and increasing pressure, as illustrated in Fig. 1. However, researchers have argued that gas hydrates (formed in a laboratory for experimental investigation) can form at moderate or ambient pressure conditions (Abbasi et al., 2021a; Abbasi et al., 2021b; Tariq et al., 2022). Furthermore, experiments replicating natural NGH conditions to investigate hydrate behaviors are conducted in high-pressure vessels (Aksnes and Kimtys, 2004; Chaouachi et al., 2015; Chen and Hartman, 2018; Haligva et al., 2010; Li et al., 2017a; Li et al., 2017b).

Several experimental techniques have been employed to investigate

the physical behavior of HBSs. For example, ultrasonic technology has been employed to elucidate primary information on hydrate formation and study the influence of ultrasonic waves on hydrate dissociation (Biot, 1955; Bu et al., 2022a; Miura et al., 2006; Winters et al., 2007). Raman spectroscopy has routinely been used to examine the structure of gas hydrates. Raman spectroscopy provides information on the structure type and can identify the phase transformation, hydration number, growth process, and other aspects (Sasaki et al., 2003; Sum et al., 1997; Uchida et al., 1995). Furthermore, the micromodels, which serve as a lab-on-a-chip (Al-Shajalee et al., 2022; Arif et al., 2019), have also been used to characterize gas hydrates. In particular, gas hydrate morphology, occurrence, and growth have been visualized using high-resolution microfluidic imaging (Almenningen et al., 2018; Mahabadi et al., 2016a; Mahabadi et al., 2016b). Microscopic and macroscopic investigations can also be conducted using nuclear magnetic resonance (NMR), a powerful tool for providing such information (i.e., morphology, occurrence, and growth). Since the 1960s, NMR has been employed in hydrate compound studies. Moreover, the capability of NMR in instant image acquisition facilitates the recording of the dynamic process of HBSs (Cha et al., 2015; Gilson and McDowell, 1961; Melnikov et al., 2012).

However, the three-dimensional (3D) spatial distribution and morphology of gas hydrate cannot be represented by any of the discussed methods. Nevertheless, it is crucial to examine the hydrate structure and growth. Thus, x-ray microcomputed tomography (μCT) has been extensively applied to produce high-resolution images of the pore structure and habits of HBSs (Gupta et al., 2009; Kneafsey et al., 2010; Seol and Kneafsey, 2009). The advancement in imaging technology is evident from the ten-fold increase in μCT acquisition speed every five years (Arif et al., 2021), indicating the promising potential of its applications. Furthermore, μCT can be combined with other techniques, such as acoustic, electrical, and mechanical measurements (e.g., scanning electron microscopy [SEM] and low-field NMR) to promote μCT technology. For instance, (Bu et al., 2022b) investigated the influence of microscopic distributions on acoustic characteristics by evaluating the elastic wave velocity and hydrate saturation during hydrate decomposition using μCT imaging. Moreover, (Bu et al., 2022a) integrated pore-scale visualization using μCT and an ultrasonic test system. These integrated systems also offer innovation to existing μCT applications. In addition, researchers have also integrated μCT with other techniques to analyze gas hydrate physical properties. For instance, (Zhao et al., 2022) combined resistivity measurements with μCT to derive the 3D spatial structure and resistivity of HBS. (Li et al., 2019b) developed triaxial
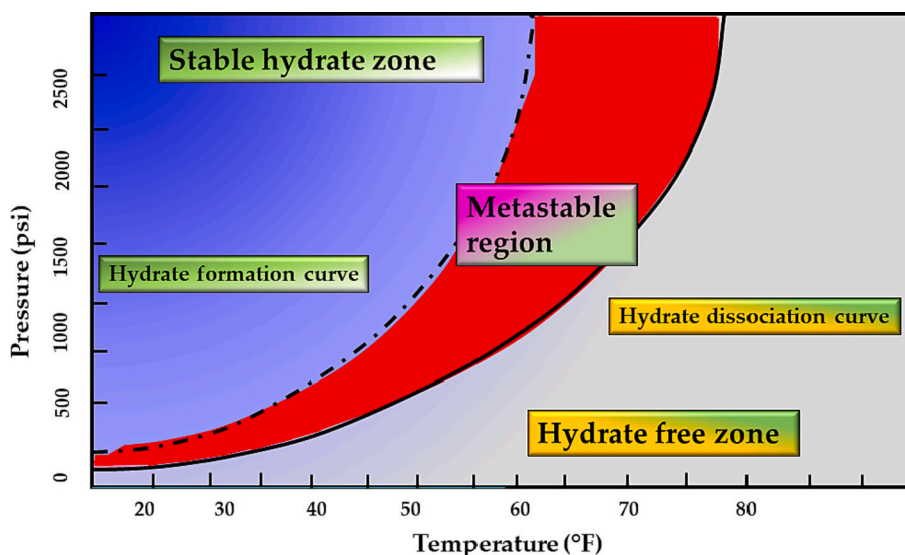

Fig. 1. Pressure-temperature curve of hydrate phases: hydrate formation and dissociation regions, modified from (Bai and Bai, 2018).

testing integrated with μCT that can record the cementation failure behavior of hydrate saturation, hydrate dissociation characteristics in HBS, and the effective stress and strain rates. (Zhang et al., 2021b) combined μCT and NMR to evaluate pore-scale characteristics. Previous reviews have focused on the feasibility of using gas hydrates as an efficient energy source (Chong et al., 2016; Liu et al., 2019; Zhu et al., 2021), the accumulation behavior of NGHs (Xie et al., 2020), and the formation and dissociation kinetics of gas hydrates (Dong et al., 2021a; Hassanpouryouzband et al., 2020; Malagar et al., 2019). In comparison, others (Ruan et al., 2021) have highlighted using numerical methods to characterize gas hydrates.

Thus, the present review focuses on the applications of μCT in gas hydrate reservoir characterization. This study presents the theoretical basis of μCT. Then, the application of μCT in NGH studies is discussed. In particular, the review emphasizes the published data on estimating hydrate saturation in porous media, hydrate pore-habit prediction, and percolation using μCT imaging. The review also provides insight into the results from studies in the last decade. Thus, this work presents a fundamental understanding of the implementation of μCT in gas hydrate characterization.

2. Gas hydrates

Gas hydrates are crystalline solids consisting of gas molecules surrounded by a water molecule cage. The hydrogen bonds connect water molecules. The gas molecules are trapped in the cage and are not bonded. The van der Waals force holds the gas molecules. Hydrogen-bonded water molecules form gas hydrates. However, gas hydrates possess different crystallographic forms stabilized by gas molecules (Dillon, 2002). Gas hydrates are usually formed by methane (CH_4). However, other hydrocarbons, such as carbon dioxide (CO_2) and hydrogen sulfide (H_2S), can also form a gas hydrate.

2.1. Physical properties of gas hydrates

Physical properties are a crucial aspect in the design of processes involving gas hydrates (Table 1). Estimating the physical properties of gas hydrates is complex because they depend upon multiple factors: the (1) hydrate type, (2) saturation degree, and (3) encaged guest molecule in the gas hydrate. The mechanical and electrical properties and heat capacity of gas hydrates are similar to those of ice. However, thermal conductivity significantly differs from ice (Handa and Cook, 1987).

(a) The molar mass (molecular weight) depends on the saturation degree and crystal structure. The molar mass also relies on pressure and temperature because the saturation degree is a function of these parameters. The molar mass of gas hydrates can be obtained using Eq. (1):

$$M = \frac{N_W M_W + \sum_{j=1}^{c} \sum_{i=1}^{n} Y_{ij} v_i M_j}{N_W + \sum_{j=1}^{c} \sum_{i=1}^{n} Y_{ij} v_i},$$ (1)

where N_W denotes the number of water molecules per unit cell, M_W indicates the water molar mass, the fractional occupancy of cavities of type I by component j is represented by Y_{ij}, vi denotes the number of type

i cavities, n reveals the number of cavities of type i, and the number of components is represented by c.

(b) Density is the mass of molecules divided by the unit volume, as presented in Eq. (2). The hydrate density is similar to that of ice; however, hydrocarbon-gas hydrates are significantly denser:

$$\rho = \frac{N_W M_W + (Y_1 v_1 + Y_2 v_2) M_j}{N_A V_{cell}},$$ (2)

where N_A represents Avogadro's number, and the volume of the unit cell is V_{cell}.

Thermal conductivity is the most crucial property of hydrates. The hydrates are significantly less conductive than ice. The thermal conductivity of hydrocarbons ranges from 0.50 ± 0.01 to 2.2 W/m K for ice. Thermal conductivity is widely considered to thaw/melt/dissociate the hydrates. Due to their low thermal conductivity value, hydrates require a longer duration to thaw.

(c) Researchers rarely study the heat capacity of hydrates. The heat capacity of hydrates is assumed constant because there is a narrow range of hydrate temperatures. The heat capacity values of hydrates are provided in the following table, where the heat capacity of ice is also included for comparison.

Other physical properties of gas hydrates include the volume of the gas hydrates and enthalpy of fusion (heat of formation).

2.2. Chemical properties and typical hydrate types and formers

Gas composition determines the structure, composition, and thermodynamic properties of gas hydrates (Table 2 and 3). The gas composition also influences the kinetics and hydrate formation. Complex mixed hydrates and simple methane hydrates have been recovered from natural sediments (Sloan et al., 2007). Complex mixed hydrates have more than one component, in which cages of the same kind are occupied by two or more molecule types, with the restriction of, at most, one molecule per cage. Simple methane hydrates have only one guest species.

Fig. 2 depicts the three structures of NGHs: Structure I (sI), Structure II (sII), and the hexagonal Structure H (sH). In addition, sI is formed by two small pentagonal dodecahedrons (5^{12}) combined with six tetrakaidecahedrons ($5^{12}6^2$). Further, sII consists of 16 pentagonal dodecahedrons (5^{12}) and eight hexakaidecahedrons ($5^{12}6^4$). The only structure comprising a cavity with three square faces and pentagonal and hexagonal faces ($4^3 5^6 6^3$) is sH, which has a combination of three pentagonal dodecahedrons (5^{12}), two irregular dodecahedrons ($4^3 5^6 6^3$), and one icosahedron $5^{12}6^8$ (Ripmeester et al., 1987; Sloan, 1998).

There are two common hydrate types (type I and II), also called structure I (sI) and II (sII), as mentioned. Another hydrate type infrequently encountered (type H) is usually referred to as structure H (sH).

The simplest hydrate structure is sI, comprising two cavities. There are 46 water molecules in sI, represented as $46H_2O + 2S + 6$ L, where S is a small molecule, and L is a large molecule. Methane (CH_4), carbon dioxide (CO_2), ethane, and hydrogen sulfide (H_2S) are common sI formers. In the ethane hydrate, the ethane molecule engages in large cavities, whereas CO_2, CH_4, and H_2S can engage in both large and small cavities.

Table 1
Gas hydrate heat capacity, based on (Carroll, 2020) and (Shicai et al., 2022).

	Hydrate type	Heat capacity (J/g °C)
Ethane	I	2.2
Methane	I	2.25
Isobutene	II	2.2
Propane	II	2.2
Ice	–	2.06

Table 2
Number of cavities per unit cell for gas hydrate structures (Sloan, 1998).

	Cavities				
	5^{12}	$5^{12}6^2$	$5^{12}6^4$	$4^3 5^6 6^3$	$5^{12}6^8$
Structure I	2	6	–	–	–
Structure II	16	–	8	–	–
Hexagonal Structure H	3	–	–	2	1

Table 3
Basic properties and hydrate formation of common natural gas components, based on (Carroll, 2020).

Hydrate	Hydrate structure	Hydrate pressure at 0 °C (MPa)	Density (kg/m^3)	Molar mass (g/mol)	Normal boiling point (K)
Carbon dioxide	I	1.208	25.56	44.01	194.7
Methane	I	2.603	19.62	2.603	111.6
Nitrogen	II	16.220	196.6	28.013	77.4
Hydrogen sulfide	I	0.099	1.50	34.080	213.5
Ethane	I	0.491	6.85	30.070	184.6
Isobutene	II	0.113	3.01	58.124	261.4
Propylene	II	0.480	9.86	42.081	225.5
Propane	II	0.173	3.49	44.094	231.1
Acetylene	I	0.557	6.70	26.038	188.4
c-Propane	II	0.0626	1.175	42.081	240.3
Ethylene	I	0.551	7.11	28.054	169.3

Comparatively, sII is slightly more complex than sI, and two cavities also form it. There are 136 water molecules in sII, represented as $136H_2O + 16S + 8L$. The most common sII formers are propane, nitrogen, isobutene, and tetrahydrofuran (THF). Propane and isobutene engage in large cavities, whereas nitrogen can engage in both large and small cavities.

An uncommon hydrate type is sH. A small molecule, such as CH_4, is required, along with an sH former, to form this hydrate type. There are three cavities and 34 water molecules in sH. To form sH, a small molecule, such as CH_4, engages in small, medium, and large cavities, whereas larger molecules (sH formers) engage in a large cavity. Theoretically, it is represented as $34H_2O + 3S + 2M + 8L$. Both sI and sII require only one former; however, sH requires two hydrate formers (e.g., CH_4, as a small molecule, and larger molecules, such as sH formers). Moreover, sH comprises the following hydrocarbons: 2-methybutane, 2,2-dimethylbutane, 2,3-dimethybutane, 2,2,3-trimethylbutane, and 2,2-dimethylpentane.
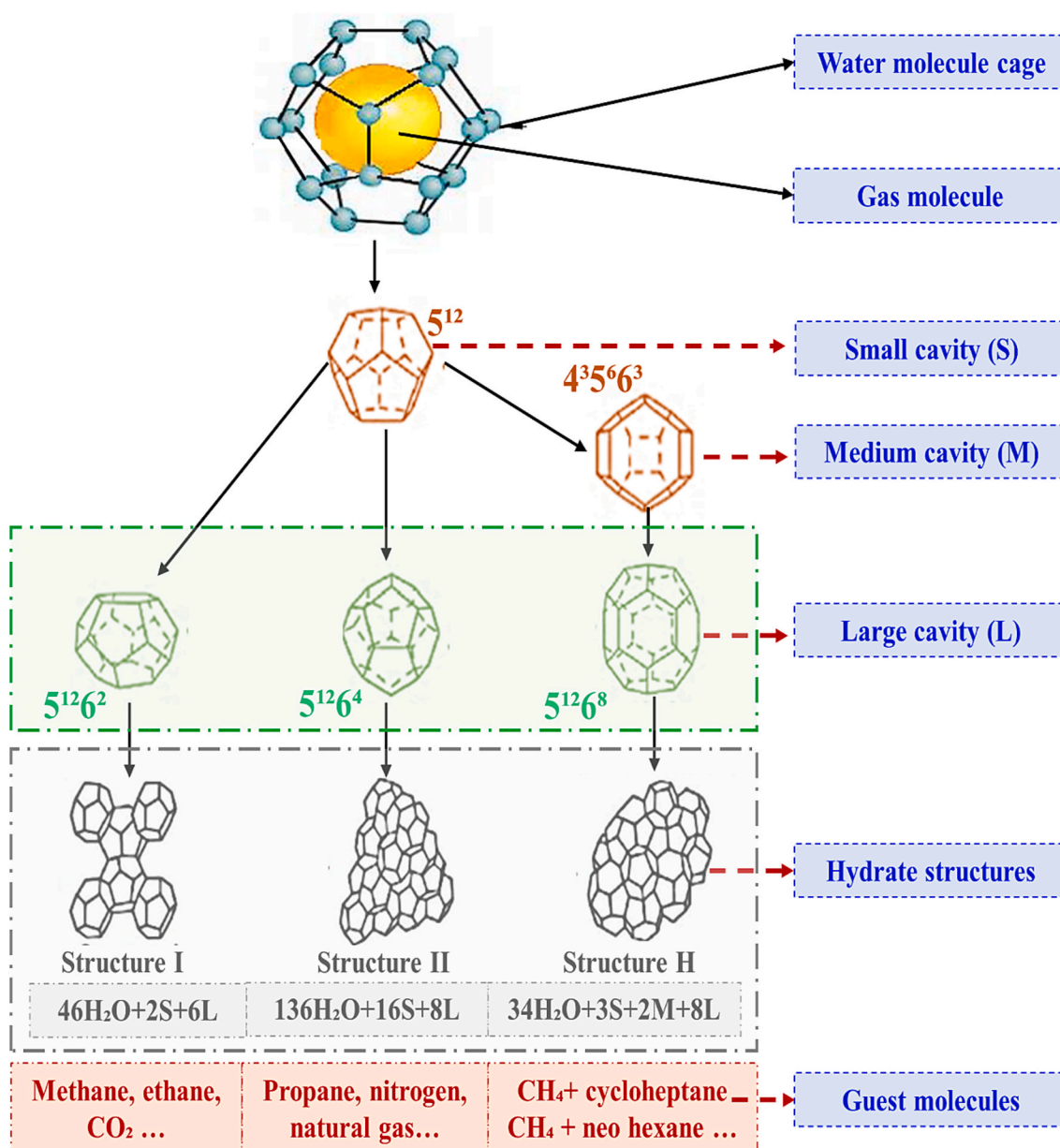

Fig. 2. Hydrate structure types: Structures I, II, and H with various molecular compositions, modified from (Strobel et al., 2009) and (Zhang et al., 2021a).

2.3. Hydrate resource occurrence

The occurrence of gas hydrates depends on low-temperature and high-pressure conditions, where the presence of gas is sufficient to initiate and stabilize the hydrate. At <2000 m subsurface depth, these conditions are met in certain regions: at (1) cold surface temperatures (<0 °C) and continental areas and (2) high pressures (>3 MPa) and cold bottom water (~0 °C) and submarine continental slopes. The worldwide occurrence of gas hydrates is presented in Fig. 3.

3. Theory of microcomputed tomography imaging

Microcomputed tomography (μCT) is a nondestructive imaging technique used to acquire 3D porous-structure imaging data and quantitatively investigate opaque systems (Cnudde and Boone, 2013; Maire and Withers, 2014). Moreover, μCT technology is based on the same principles as those applied in medical computerized axial tomography. As the radiation of the x-ray beam passes through the sample, it experiences continuous attenuation due to the absorption of the constituent atoms (Li et al., 2019a). A relationship between the x-ray transmission intensity, incident radiation, and linear absorption coefficient is provided by Lambert-Bee's equation:

$$I_l = I_o e^{-\mu d}, \tag{3}$$

where I_o represents the x-ray transmission intensity, I_l denotes the incident radiation, μ is the linear absorption coefficient, and d is the thickness of the sample (Maser, 2001).

The x-ray transmission intensities can be measured using a complementary metal–oxide semiconductor and charge-coupled devices (Chung et al., 2019). The CT number N is reported by the CT image given by Eq. (4):

$$N = c.(\mu.\mu_w)/\mu_w, \tag{4}$$

where μ_w represents the linear absorption of water, and c denotes a scaling constant (Li et al., 2017a; Li et al., 2017b). The gray value contrast between various phases produces the different attenuation used in CT. Different N values describe the gray level of various matters in CT images, such as −1000 for air and 0 for pure water.

3.1. Microcomputed tomography experimental setup

A synchrotron-based μCT and a cone-beam or fan-beam lab-based μCT are the most common types of μCT setup. The cone-beam μCT uses geometrical magnification by placing the sample between the detector and x-ray source for examination. The highest attainable resolution (<1 μm) can be achieved with microfocus x-ray tubes (Cnudde and Boone, 2013; Maire and Withers, 2014; Mees et al., 2003). In contrast, synchrotron-based μCT generates a parallel x-ray beam that transits via the monochromators using a bending magnet. A scintillator screen detects the beam after transmitting the sample that transforms the x-rays to light. Visualizing optics are employed to magnify the image on a detector, such as a complementary metal–oxide semiconductor or charge-coupled device camera. A high resolution can be attained with a voxel size of ~10 nm (Chao et al., 2005; Dierolf et al., 2010; Godard et al., 2011) using coherent diffractive imaging. The experimental lab-based μCT setup schematic diagram is presented in Fig. 4.

3.2. Three-dimensional visualization

A reconstruction approach can be used to compute the x-ray attenuation inside a stack of 2D slices after radiographic projections of the sample have been obtained. Some software packages, such as 3DMA, Fiji, and Avizo, can reconstruct the 3D sample (Ketcham, 2005; Lindquist et al., 2000; Schindelin et al., 2012). Artifacts and noise in μCT imaging can occur during data acquisition (Blunt et al., 2013; Ketcham and Carlson, 2001; Mathews et al., 2017; Saxena et al., 2017; Van Geet et al., 2000). Usually, some practices are conducted to reduce or diminish them before the segmentation process (Blunt et al., 2013; Mathews et al., 2017; Otsu, 1979). Moreover, before presenting the raw data for the reconstruction process, numerous mathematical filtering methods enhance the signal-to-noise ratio of the data (Cnudde and Boone, 2013; Mathews et al., 2017). Moreover, μCT is a powerful tool for quantitative investigation because it enables 3D data visualization, such as grain analysis and pore-system characterization (Cnudde and Boone, 2013; Van Geet et al., 2000). Further, μCT imaging quantifies the internal rock structure and high-resolution computations using a quantitative investigation to determine the pore geometry, mineral assemblages, pore-size distribution, fracture-aperture distribution, and porosity (Dong et al., 2021b; Isah et al., 2022).
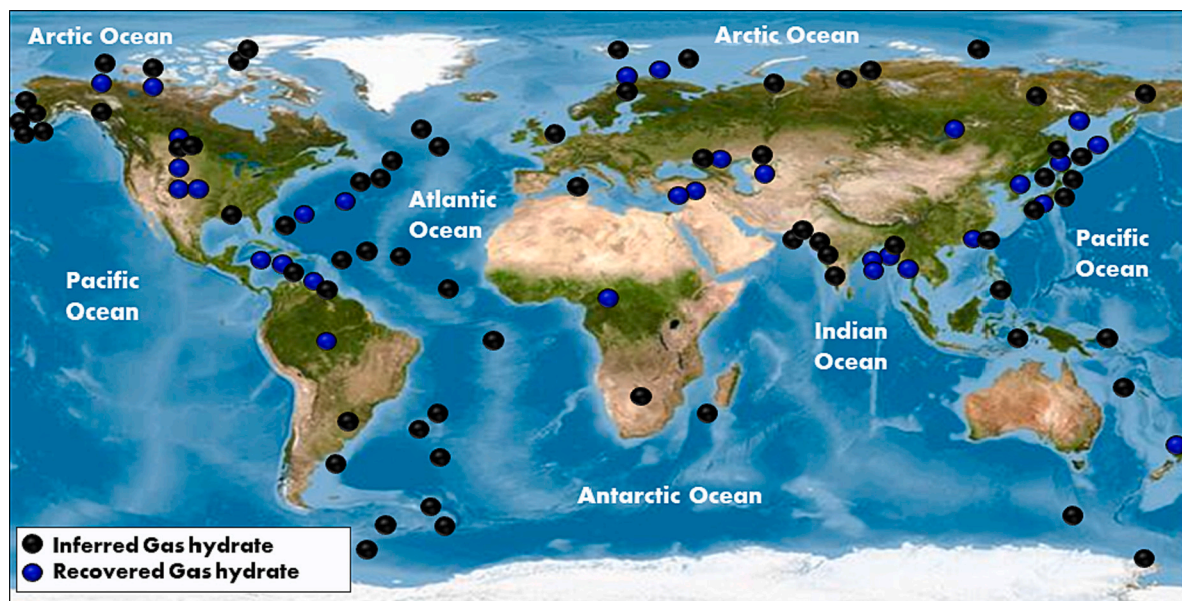

Fig. 3. Map presenting gas hydrate locations. Modified from (Yan et al., 2020).
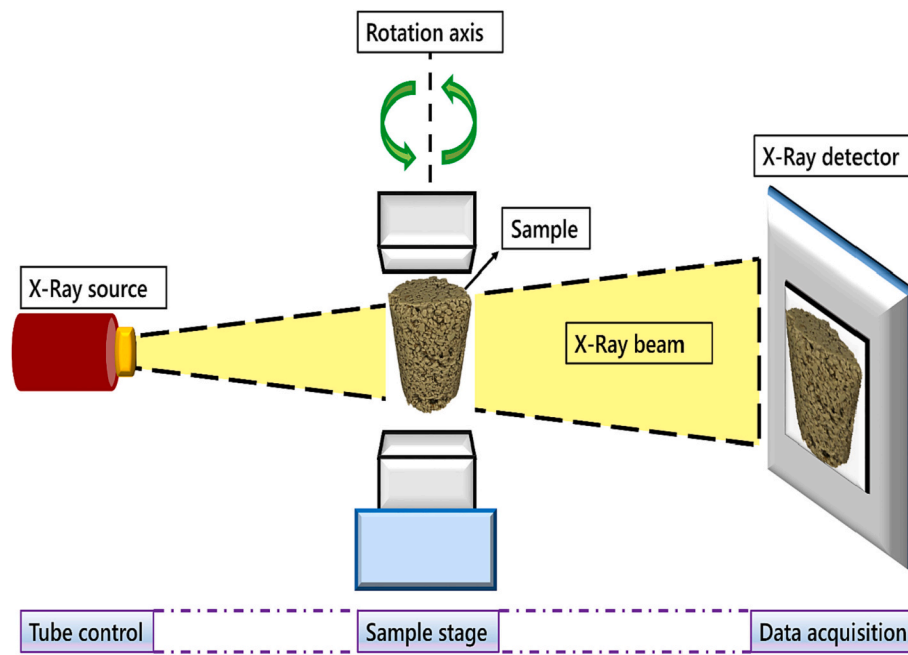
Fig. 4. Schematic diagram of the microcomputed tomography apparatus, modified from (Liu et al., 2021b).

4. Gas hydrate characterization using microcomputed tomography imaging

For a better understanding of gas hydrate formation and the dissociation mechanism, it is essential to analyze the pore-habit alteration, saturation and percolation behavior, and permeability and seepage characteristics that cannot be observed using traditional methods. In addition, μCT can provide direct visualization of the hydrate structure; hence, it is extensively used in hydrate studies. The following sections discuss and critically review the current literature on gas hydrates using μCT.

4.1. Gas hydrate pore-habit predictions using microcomputed tomography

This section reviews the literature available in the past decade on using μCT on hydrate pore habit, growth, and occurrence (Table 4). The appearance of NGH is affected by several factors, such as the pore-throat diameter, local capillary force, wettability, and pore-surface roughness. Currently, there are limited studies of the hydrate growth pattern in sediments. Researchers have often assumed different growth patterns and conducted experiments covering possible hydrate pore habits.

The μCT technique can identify the NGH phase spatial distribution in the pores. (Zhao et al., 2016) executed methane hydrate formation experiments and used three sizes of sand particles (2.85 to 4.8 mm, 1.18 to 2.85 mm, and 0.85 to 1.18 mm). The authors observed hydrate formation in the pore space and along the surface of the sand particles. The hydrate growth pattern is random in the pore space during hydrate formation; however, hydrates are primarily present in the pore space without contacting the pore surface; thus, hydrate pore filling can advance in all directions. This mode of hydrate filling in porous media is called a floating model (Sadeq et al., 2018; Yang et al., 2018). The surrounding medium is compacted due to hydrate formation because hydrate formation extracts water from sediments. This effect is due to the temperature decline in the pressure-temperature curve of the hydrate phase diagram (see Fig. 1).

Moreover, (Lei et al., 2019) published comprehensive research on methane hydrate formation over 13 days. However, they declared that hydrate grows over the surface of sand particles and usually forms a network in the 3D volume. The NGH usually forms an inhomogeneous

distribution in the pore space. Several researchers have reported an inhomogeneous hydrate distribution in partially and fully brine-saturated porous media (Schindler et al., 2015; Yang et al., 2016a; Yang et al., 2016b; Yang et al., 2016c). (Schindler et al., 2015) reported partial hydrate contact with grain at a higher hydrate saturation. Fig. 5 indicates that hydrate formation occurred in the pore space and seemed connected between the grains. This process is attributed to the initial growth at the grain surface, connecting by slowly growing in the pore space.

Furthermore, different shapes of hydrate growth are found in porous media, and spike shapes appear in gas pockets in several spots. This shape has been termed *soda straw stalactites* and *ice spikes* by various researchers (Libbrecht and Lui, 2004). An essential factor for hydrate formation is the growth rate. In addition, μCT can calculate the growth rate in a high-pressure vessel. The decline in hydrate growth rate is observed initially and rises dramatically with overpressure and undercooling.

Hydrate nucleation (the initial process of hydrate formation involving the arrangement of the constituent particles into hydrate crystal) is promoted by the presence of clay minerals. The induction time with clay is 180 min less than without clay (Lei et al., 2019; Lei and Seol, 2020). The presence of sodium dodecyl sulfate (SDS) in an appropriate amount (300 ppm) also promotes the induction time of hydrate formation. A low concentration of SDS decreases the bubble size, expanding the effective mass transfer area; thus, the process of hydrate formation advances. At a high SDS concentration, the interfacial adsorption of SDS has a dominant effect and impedes the gas molecule diffusion from the gas to the liquid phase (Lv et al., 2020). Thus, the promoting efficacy of SDS on hydrate formation is restricted.

4.2. Gas hydrate saturation and percolation behavior using microcomputed tomography

This section discusses the use of μCT to investigate the saturation and percolation behavior of HBSs Table 5. The movement of a fluid through a fully interconnected network is called percolation. Hence, percolation is the flow behavior of HBSs. Percolation behavior is affected by several factors, such as permeability, porosity, hydrate saturation, wettability, pore size, and capillarity (Daigle, 2016; Wang et al., 2020). It is

Table 4
Available literature on gas pore-habit predictions using microcomputed tomography.

Reference	Hydrate	Porous media	Aqueous phase	Temperature (K)	Pressure (MPa)	Remarks
(Zhao et al., 2016)	Methane	Sand (0.85–1.18, 1.18–2.85, and 2.85–4.8 mm)	Deionized water	274–281	5.9–6.0	• Uniformly distributed hydrate • Hydrate completely fills the pores
(Chen and Hartman, 2018)	1. Xenon 2. Methane 3. Xenon	1. No porous medium 2. Water droplets 3. Wet sand pack	Deionized water	1. 296.15 2. 274.14 3. 296.35	1. 2.84 2. 7.05 3. 3.72	• Pore-habit changes from grain attaching to pore filling with increased hydrate saturation • High hydrate saturation promotes grain cementation
(Bu et al., 2022b)	Methane	Sand	NaCl	274.95	4	• Gas hydrate dissociates as a pore-filling model, and hydrate micro-distribution is the main factor affecting the acoustic wave velocity
(Jin et al., 2014)	Methane	Artificial sediments		243	10	• Porosity and hydrate saturation are varied to analyze grain cementation
(Lei and Santamarina, 2018)	CO_2	Six sediments	Deionized water			• When the mineral is hydrophilic, the pore habit is not pore filling but cementing
(Lei et al., 2019)	CO_2	Sand and clay sand ranges (0.8–1.22 mm)	Deionized water	274.65	3.3	• Clay minerals accelerate hydrate nucleation and growth
(Lei and Seol, 2020)	Methane	Sand	Deionized water	277.65	13.75	• Hydrate in the hydrophilic system develops as pore filling
(Rees et al., 2011)	Methane	Reservoir hydrate sample and laboratory sand packs	Deionized water	276.4	4.36	• Nucleation of hydrate occurs randomly with many parameters, such as saturation, salinity, pore-size distribution, and mineralogy, affecting the nucleation process
(Sadeq et al., 2018)	CO_2	Bentheimer	Sodium iodine brine	274	3	• Gas hydrate forms as a free-floating model
(Schindler et al., 2017)	Tetrahydrofuran	Borosilicate glass beads	Deionized water mixed with barium chloride	277.15	1	• Hydrate-bearing sediments follow the pore-filling model
(Ta et al., 2015)	CO_2	Borosilicate glass beads	Potassium iodine solution	275.15	3	• Nucleation occurs at the grain surface
(Yang et al., 2015)	Methane	Quartz glass sand	Deionized water	274.15	7	• The occurrence is like a floating model
(Yang et al., 2016b)	Methane	Glass beads	Deionized water	274.15	6	• Hydrate occupies random pores
(Yang et al., 2016a)	Xenon	Quartz sand (200–300 μm)	Brine	276	0.4	• Grain-coating hydrates have higher permeability than pore-filling models at specific hydrate saturations
(Liu et al., 2021a)	Xenon	Sand sediments	NaBr solution	296.15	3.6	• Grain-coating hydrates have higher relative permeability than pore-filling gas hydrates
(Sun et al., 2021)	Xenon	Sand pack	Brine (10 wt% NaBr)	296.15	3.5–3.7	• Grain-coating hydrates form at low hydrate saturation
(Dong et al., 2020)	–	Sandstone	NaCl solution	–	–	• In adhesive mode hydrate, resistivity values are high • In scattered mode, resistivity values are low
(Chen et al., 2022)	Methane	Sediment	NaCl solution	273.15	4.9	• The quantity of gas hydrate particles greatly influences the pore network. For instance, too many gas hydrate particles hinder the pore network blocking.

Note: CO_2 = carbon dioxide; NaCl = sodium chloride; NaBr = sodium bromide.

generally agreed that hydrates grow (thus, increasing hydrate saturation) and percolate within porous media. However, different modes of saturation changes and the percolation behavior of gas hydrates have been reported by various researchers based on their experimental observations and numerical analyses (Fig. 6).

Microcomputed tomography scanning is a nondestructive method for obtaining detailed observations of hydrate formation and fluid migration and insight into the changes in hydrate saturation within HBSs. (Wang et al., 2018b) studied methane hydrate formation in sand samples. Their results demonstrated that hydrate grows in grain-cementing mode except in some cases, where pore-filling and floating models were observed. In another study, (Wang et al., 2015a) conducted experiments on methane hydrate formations in a sand sample (Fig. 7). They observed a thin layer of free water between the sand grains and hydrate and stated that the hydrate does not adhere to the pore walls. They noted that NGH grows in pores in the pore-filling model.

Moreover, (Seol and Kneafsey, 2011) conducted an experimental study and numerical simulations of methane hydrate formation in an unsaturated sand sample. The authors suggested that hydrate behaves as a pore body–filling hydrate accumulation. This pore-filling behavior is attributed to increased hydrate saturation, which decreases the average

pore and throat radii (Wang et al., 2015a). However, (Sadeq et al., 2018) performed experiments on CO_2 hydrate in Bentheimer sandstone. The reported CO_2 hydrate predominantly grows in pores at the gas–water interface without contacting the grain surface. They also measured the P-wave velocities, revealing an increase of 7% to 8% after hydrate formation, verifying the hydrate-free-floating behavior. Furthermore, (Zhao et al., 2014) observed a water layer coating the grains. They found that gas hydrates formed randomly in the pore space instead of contacting the grain surface, which is consistent with the findings by (Sadeq et al., 2018).

4.3. Gas hydrate saturation and mechanical behavior

Hydrate saturation, the proportion of hydrate in the pore space volume, is discussed by several researchers of HBSs (Table 6). However, researchers have rarely explored the interplay between the hydrate saturation and mechanical behavior of HBSs using μCT; therefore, we highlighted the available literature in recent years on various hydrate saturation phases and the corresponding mechanical characteristics of the HBS using different modern instruments. Moreover, modern instruments and techniques depict multiple benefits of analyzing the
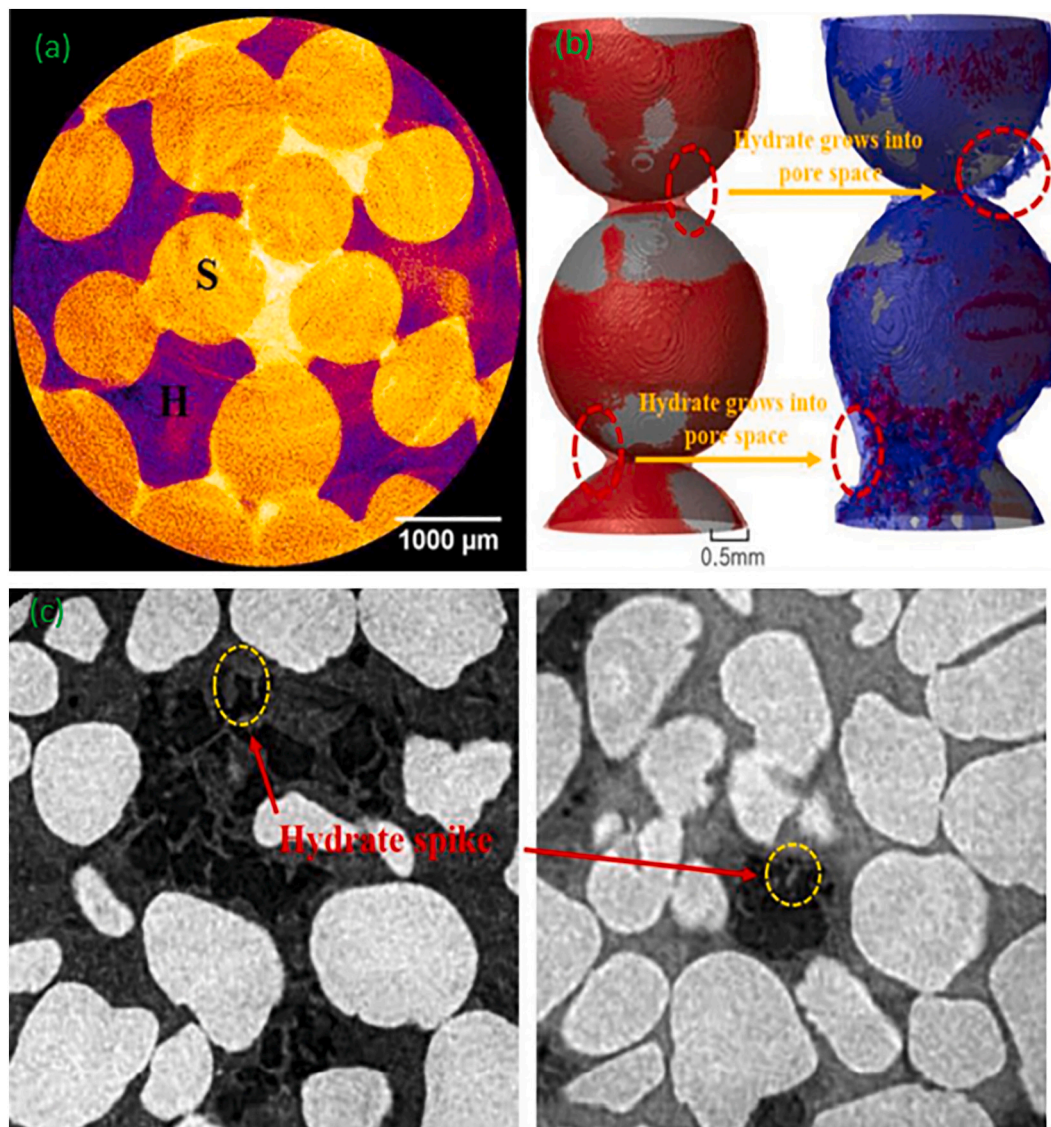
Fig. 5. Gas hydrate growth pattern in porous media using microcomputed tomography: (a) hydrate bridge, (b) hydrate growth on the surface, and (c) hydrate spike shape. Adapted from (Lv et al., 2020) with permission from Elsevier.

formation mechanisms, microstructural properties, and thermal physical properties of gas hydrates. Various techniques have been successfully incorporated into gas hydrate-related research with the advancement of specialized experimental tools.

Fig. 8 presents four hydrate saturation phases: hydrate-free sediment, low hydrate saturation, intermediate hydrate saturation, and high hydrate saturation. The pore-scale behavior of the sand particles during the shearing process for hydrate-free sediments is primarily governed by the energy principle, and the sand particles could reorganize to control the increased shear stress and friction by slippage, rotation, and other means (Wu et al., 2020). However, crushing and breakage may occur when the shear stress surpasses the strength of the sand particle, resulting in a significant decline in the strength of the sediment.

Moreover, dilation occurs in dense sediments (fine particles), and compaction occurs in loose sediments. In low hydrate saturation, hydrate saturation has less effect on the strength due to the low hydrate volume. The hydrate formation is on the surface of the sand particle without being in contact with other particles. Hence, the hydrate cementation strength is lower than the shear stress, and the influence of the hydrate on the sediment strength is finite (Kajiyama et al., 2017). The volumetric dilatancy can be escalated considerably because the crushed and broken hydrate particles occupy the surrounding pore space to increase the sediment density. In the case of high hydrate saturation, the sand particle rearrangement is hindered by pore-filling and cementing hydrates.

Because of the formation of the skeleton, the hydrate cementation strength could be significantly improved in the initial state once the generated hydrate particles attach (Wu et al., 2020). Typically, the formation of a large hydrate cementer cluster occurs, making rearrangement and rotation challenging during the shearing process. When the hydrate-sand bonding strength is greater than the hydrate cementation strength in these clusters, a shear plane forms through the hydrate mass, and the mechanical properties of the hydrate dominate the HBS strength evolution (Wu et al., 2020). This outcome is primarily anticipated in sediments with low specific surface areas and rough surfaces (Wu et al., 2020). Thus, when the cementation strength exceeds the hydrate-sand bonding strength, failure emerges along the hydrate-sand interface, and several hydrate particles appear along the shear plane due to shearing, resulting in more noticeable strain dilation and softening. This result is more anticipated in HBS with high specific surface areas or smooth surfaces than in others (Yun et al., 2007).

Table 5

Available literature on gas hydrate saturation and percolation behavior using microcomputed tomography.

| Reference	Hydrate	Porous media	Aqueous phase	Temperature (K)	Pressure (MPa)	Remarks
(Wang et al., 2016b)	Methane	Quartz glass beads	Deionized water	273.35	5.6	• With increased grain diameter, the porosity of porous media comprising hydrate also increases
(Wang et al., 2015a)	Methane	Quartz sand	Deionized water	273.35	5.6	• Hydrate grows as a pore-filling model
(Seol and Kneafsey, 2011)	Methane	Sand pack	Water	281	8.3	• Hydrate accumulates as a pore-filling model subject to hydrate-bearing sand water injection
(Seol et al., 2006)	Methane	Sand	Water	276	4.5	• The heterogeneity of hydrate saturation causes differences in relative permeability and capillary pressure of hydrate-bearing sediment
(Sadeq et al., 2018)	CO_2	Bentheimer	Brine	274	3	• CO_2 hydrate forms as a free-floating model, attributed to increased P-wave velocities
(Wang et al., 2018b)	Methane	Sand	Deionized water	275	4	• Hydrates grow as a grain-cementing model • At intermediate stages, gas hydrate can grow as a pore-filling model • Gas hydrate formation significantly influences flow properties
(Al-Raoush et al., 2019)	CO_2	Silica sand	–	–	–	• With increased fine concentrations, gas percolation decreases, and regardless of the wetting phase, pore and throat diameters decrease, which is attributed to the dislocation in the sand • Sand-brine interfaces accumulate hydrophobic particles, and the brine-gas interface includes hydrophilic clay
(Zhao et al., 2014)	CO_2 + Methane	Glass beads	Water	276 for CO_2, 274 for methane	5 for CO_2, 7 for methane	• Gas hydrate growth occurs in the free-floating model
(Zhao et al., 2015)	Methane	Silica sand	Deionized water	274	8	• Regardless of the wetting phase and grain size, hydrates nucleate as lens-shaped clusters

Note: CO_2 = carbon dioxide.
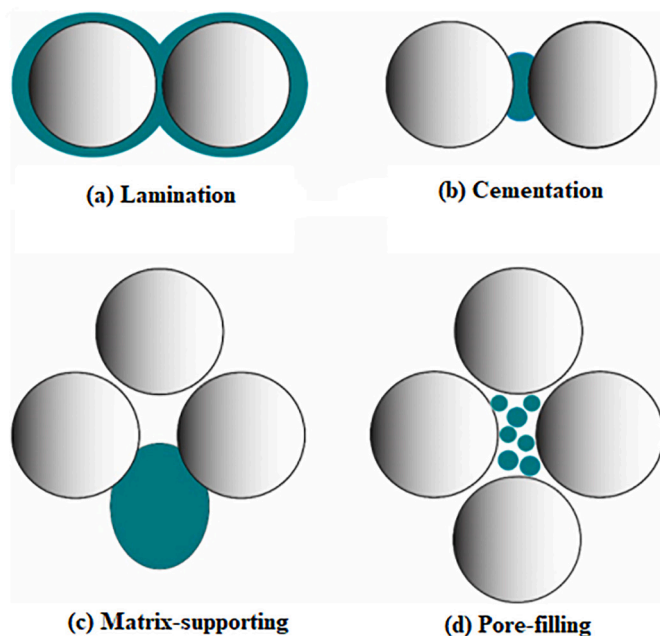
Fig. 6. Hydrate filling modes: encrustation/coating (laminating), cementing, matrix supporting, and pore filling; adapted from Sell et al. (2016).

4.4. Gas hydrate permeability/seepage using microcomputed tomography

Seepage characteristics of HBS play an essential role in accurately estimating natural gas production and characterizing fluid behavior in exploiting gas hydrate resources (Table 7). The relative permeability of the gas and water phase and the porous media is critical among these seepage characteristics, and μCT can present a detailed understanding of hydrate morphology, which is a critical factor for calculating permeability. Furthermore, μCT scans can provide an accurate and integrated pore structure of HBSs for advanced numerical simulations for permeability prediction. The available literature in the past 10 years on seepage characteristics of HBSs using μCT is discussed in Table 7. In the following paragraphs, we discuss studies examining the seepage characteristics of HBSs employing μCT.

Permeability laboratory measurement methods are primeval and usually conducted in cylindrical press–volume–temperature (PVT) vessels. In addition, μCT experiments are employed to observe the flow behavior of a gas/water flooding test in HBSs. For instance, (Seol et al., 2006) used methane-hydrate-saturated consolidated sand packs (fine) to estimate gas permeability. They applied the gas flow through the consolidated fine sand packs and measured the pressure variation at both ends of the PVT vessel. A water flooding test was conducted to investigate the water-flow behavior in HBSs. The variation in saturation was observed at fixed spots using μCT. The results indicate that the water-flow behavior deviates from higher porosity to higher hydrate saturation.

(Kneafsey et al., 2010) reported a more complex water-flow behavior. They stated that the water-flow path improves at higher hydrate saturations with increased local capillary suction on some occasions. In many cases, water flow is obstructed, and the relative permeability of gas is low at higher hydrate saturations because gas hydrates engage most of the pore space. In addition, μCT scanning was used to detect the displacement front of injected water in a core holder, which was correlated with the adjustment in the differential pressure of each layer in the core holder. A precise prediction of the effective permeability of the water/gas phase was obtained by removing the capillary end effect with this method.

In core-flooding experiments, the precision and reliability of the measured permeability values are limited due to the nature of the flow law, location of the μCT observation area, core size, and experimental conditions. Many advanced simulation models have been employed in studies to predict the permeability of HBSs to resolve these challenges. The pore network model is one of the numerical models capable of evaluating the 3D percolation properties of gas, water, sand, and hydrate. The advancement in μCT techniques has benefited the pore network model. Thus, the permeability progress during hydrate formation/dissociation is better simulated, and more accurate permeability measurements for the water/gas phase are acquired.

(Wang et al., 2018a; Wang et al., 2015a; Wang et al., 2015b; Wang et al., 2016a) conducted extensive research on the seepage properties of water/gas flow in HBSs using μCT imaging in conjunction with the pore network model. In a high-pressure vessel containing consolidated quartz
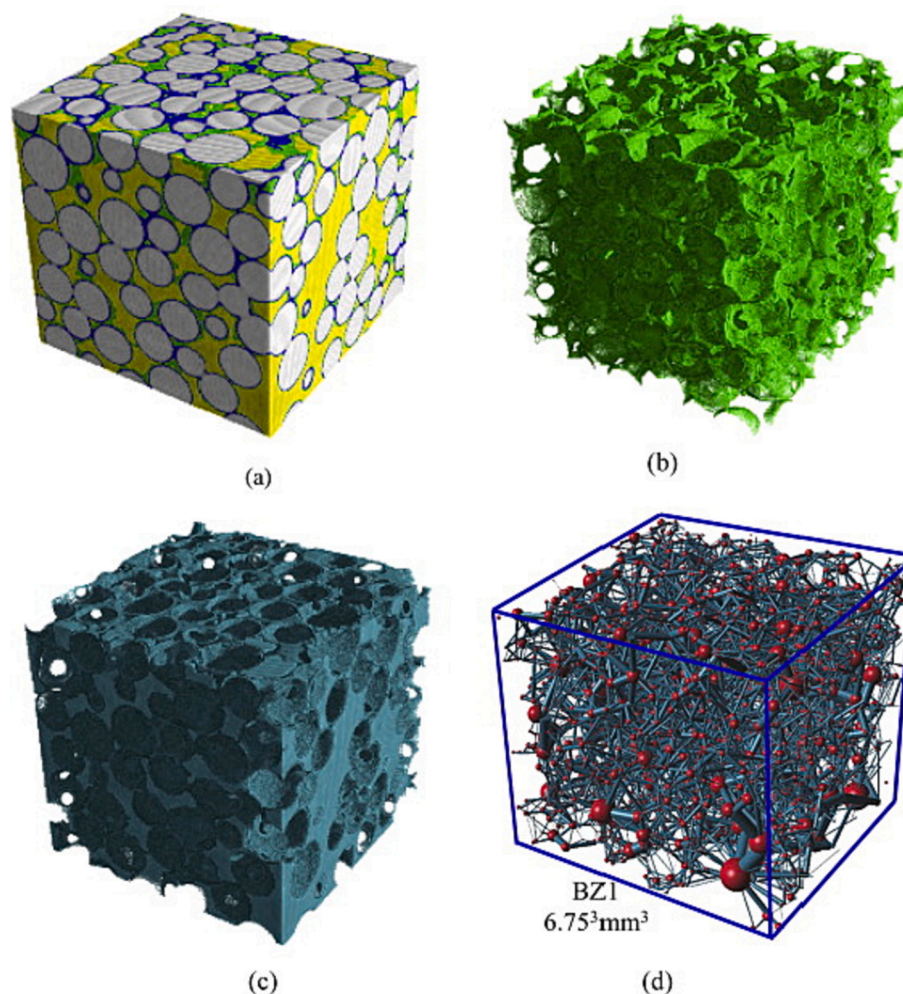
Fig. 7. (a) Core sample, (b) methane hydrate in pore space, (c) fluid flowing in pores, and (d) generated pores and throats, adapted from (Wang et al., 2015a) with permission from Elsevier.

sand packs, methane hydrate was fully formed. Dong's maximal ball method was used to extract pore structure information from HBSs preserved by μCT images, which was derived from (Silin et al., 2003) and the maximal ball concept (Zhang et al., 2020).

The extraction of the pore network model from the original μCT images is depicted in Fig. 9. The simulation of the pore network model revealed that the capillary pressure increases with methane hydrate saturation. Conversely, the relative and absolute permeability of the water phase were inversely proportional to the hydrate saturation. (Wang et al., 2016a) further studied the wettability influence and particle size effect on the permeability of HBSs. They reported that water-phase relative permeability was negatively correlated with the hydrophilicity of the porous media under the same conditions. (Yang et al., 2018) investigated the inhomogeneity of the porous media using three compositions of minerals (quartz, dolomite, and feldspar). The anisotropy of pore structures causes the difference in permeability. Higher absolute permeability was achieved in smaller pore/throat ratios. This outcome demonstrates that the absolute permeability is low due to the complex pore structures of HBSs.

4.5. Other experimental investigations on gas hydrates

The physical and chemical properties of gas HBSs are critical parameters for producing gas hydrate. Gas hydrate production is significantly dependent on proper experimental analyses and simulations. Some properties of gas hydrates can be examined with natural samples,

and the specifications of the gas hydrate characteristics can be acquired by investigating hydrate samples. Moreover, experiments provide an overview of gas hydrates. This section provides a concise discussion on gas hydrate characterization using various techniques.

Studying physical and chemical properties is crucial to understanding gas hydrate behavior. The primary focus of conventional gas hydrate evaluation techniques is pressure, temperature, and saturation (Wu et al., 2018). Modern techniques, including x-ray CT, SEM, Raman spectroscopy, high-pressure differential scanning calorimetry (DSC), x-ray diffraction (XRD), and NMR, have been applied to study the formation and dissociation mechanisms; structural analysis; physical, chemical, and thermal properties; and phase equilibrium of gas hydrates. Many methods have been successfully implemented with the advancements in experimental tools in studies related to gas hydrates.

Microstructures of gas hydrates have been successfully studied using NMR, XRD, and Raman spectroscopy. A basic study of gas hydrate has been conducted using Raman spectroscopy, which is most suitable to deduce hydrate existence, its molecular composition, cage occupancy, and structure type. The hydrate number and structural type can be obtained by examining the chemical bonds of water molecules (O—H bonds) and guest molecules (C—H bonds and C—C bonds). Both NMR and XRD are crucial tools for identifying the structure type, formation and dissociation kinetics, and gas storage performance (Zhang et al., 2017). The hydrate space groups, crystal structure, cavity occupancy, hydration index, and lattice parameters can be determined using XRD. For the multicomponent hydrate structure type, NMR is a powerful

Table 6

Available literature on hydrate saturation estimation using different observation methods.

Reference	Porous media	Aqueous phase	Hydrate	Remarks
(Miyazaki et al., 2011)	Silica and Toyoura sand	Saturated with water	CH_4	• With increased hydrate saturation, the strength and stiffness of hydrate-bearing sediments also increase
(Masui et al., 2005)	Toyoura sand	Saturated with water	CH_4	• The cohesive contact between sand and hydrate influences the strength of hydrate-bearing sediments
(Abbasi et al., 2021b)	Bentheimer	Saturated with water	THF	• At the same temperature–pressure conditions, water-wet sandstone has a higher hydrate saturation than oil-wet sandstone
(Yun et al., 2007)	Silt, clay, and sand	Saturated with water	THF	• The stress-strain behavior of hydrate-bearing sediment depends on the confining pressure, particle size, and hydrate concentration
(Yoneda et al., 2016)	Toyoura sand	Saturated with gas	Kr	• Internal friction increases due to hydrates in the pore space, and the strength and stiffness are governed by hydrates at the menisci
(Miyazaki et al., 2016)	Toyoura sand	Saturated with water	CO_2	• The strength of CO_2 hydrate sands was less than that of the CH_4 hydrate samples at high hydrate saturations
(Ghiassian and Grozic, 2013)	Ottawa sand	Saturated with water	CH_4	• The hydrate-bearing sediment strength is significantly affected by the hydrate morphology
(Wang et al., 2019)	South China Sea clayey silt	Saturated with gas	CH_4	• High hydrate saturation has a high internal friction angle, strength, cohesion, and stiffness of hydrate-bearing sediments
(Hyodo et al., 2014)	Toyoura sand	Saturated with water	$CH_4 + CO_2$	• The initial stiffness of the CH_4 hydrate-bearing sediment was higher than that for CO_2 hydrate-bearing sediment under similar hydrate saturation
(Hyodo et al., 2013)	Toyoura sand	Saturated with water and gas	CH_4	• In gas saturation, hydrate-bearing sediment stiffness and strength are higher than in water saturation
(Dong et al., 2020; Dong et al., 2019)	Fujian sand	Saturated with gas	CH_4	• Hydrate distribution significantly affects the stress-strain of hydrate-bearing sediments

Note: CH_4 = methane; THF = tetrahydrofuran; CO_2 = carbon dioxide; Kr = krypton.

method and highly sensitive; therefore, it helps investigate the gas molecule dynamics and chemical behavior of different gas hydrates. Hence, NMR can be employed to study gas hydrate formation and dissociation kinetics and structure information (Fu et al., 2017; Meng et al., 2011b; Meng et al., 2015b).

Researchers in several areas of China have employed Raman spectrometry and XRD to study gas hydrates (Liu et al., 2015; Liu et al., 2017; Liu et al., 2012; Liu et al., 2010a; Meng et al., 2011a; Meng et al., 2015a). Their results revealed that most hydrates form sI and accumulate 99% of methane gas. The shift from thermodynamics to kinetic measurements is challenging for researchers (Wu et al., 2018). Magnetic resonance imaging (MRI) and CT are used to study the microscopic kinetics of hydrates in HBSs. The key parameters that control the growth and nucleation of hydrates in the pore space can be investigated microscopically using these instruments. The study of the formation and dissociation mechanism, evaluation, and exploration of gas hydrates is related to understanding the occurrence of gas hydrates. X-ray CT can be used to observe the microscopic distribution of hydrates in porous media and investigate the dissociation mechanism and internal spatial structure of HBSs. The kinetics and formation dissociation mechanisms and microscopic distribution have been investigated by researchers using x-ray CT (Hu et al., 2014; Jiang et al., 2005; Li et al., 2013; Pu et al., 2007; Wang et al., 2015a; Wu et al., 2006; Zhang et al., 2016).

In addition, MRI reveals a brightness difference between the solid hydrate and free water, which depicts the hydrate formation and dissociation. Proton density affects the MRI signal. Hence, MRI differentiates the phase states and produces quantifiable data for porosity, fluid distribution, pore-size distribution, and variation in hydrate saturation in the pore space. Several researchers have used MRI to investigate hydrate formation, dissociation, kinetics, saturation, fluid migration, and behavior in porous media (Liu et al., 2010b; Qingguo et al., 2012; Yao, 2010).

Furthermore, neutron scattering has also been extensively applied to investigate the gas hydrate structure (Hosseini et al., 2021). For instance, gas hydrate formation and dissociation have been quantified, which is significant in the hydrate "gun" hypothesis and unconventional fuel resource recovery. Furthermore, neutron scattering can be employed at high gas pressures, which exist in gas hydrate formations (Hosseini et al., 2021).

High-pressure and low-temperature reactors have been employed to study the phase equilibrium of gas hydrates. Phase equilibrium data with various components are acquired in abundance from gas hydrates (Du et al., 2011; Fan et al., 2001; Liang et al., 2001; Litao et al., 2009; Sun et al., 2010; Sun et al., 2002a; Sun et al., 2002b; Sun et al., 2001). Hydrate phase equilibrium data were obtained by (Ma et al., 2008) from systems comprising methane, hydrogen, ethylene, and ethane in the presence and absence of THF in water. Their results indicated that hydrogen could be successfully separated from other gases by forming a gas hydrate. (Litao et al., 2009) also observed hydrate phase equilibrium data from various solution systems.

High-pressure DSC is becoming prominent in investigating the hydrate phase equilibrium over the past few years because the contemporary PVT reactors are challenging to use, and the obtained data are usually ambiguous. The heat flux estimation during a hydrate phase change can be performed under high-pressure conditions by employing high-pressure DSC. Accordingly, specific heat and thermal dissociation equilibrium data can be acquired under the desired conditions. (Chen et al., 2012) investigated the phase equilibrium of hydrates in porous media and pore water using this method. Their results indicated that, with a pressure range from 10 to 30 MPa, the temperature of the hydrate phase equilibrium is approximately 2 K lower than that in pure water. However, this requires more study under specific conditions at sea.

5. Recommendations

While significant progress has been achieved in using μCT technology to evaluate hydrate pore behaviors and characteristics, we highlighted some areas that require further investigation:

- A limitation of the μCT technology is that the sample size should be small enough to acquire high-resolution images, which are essential
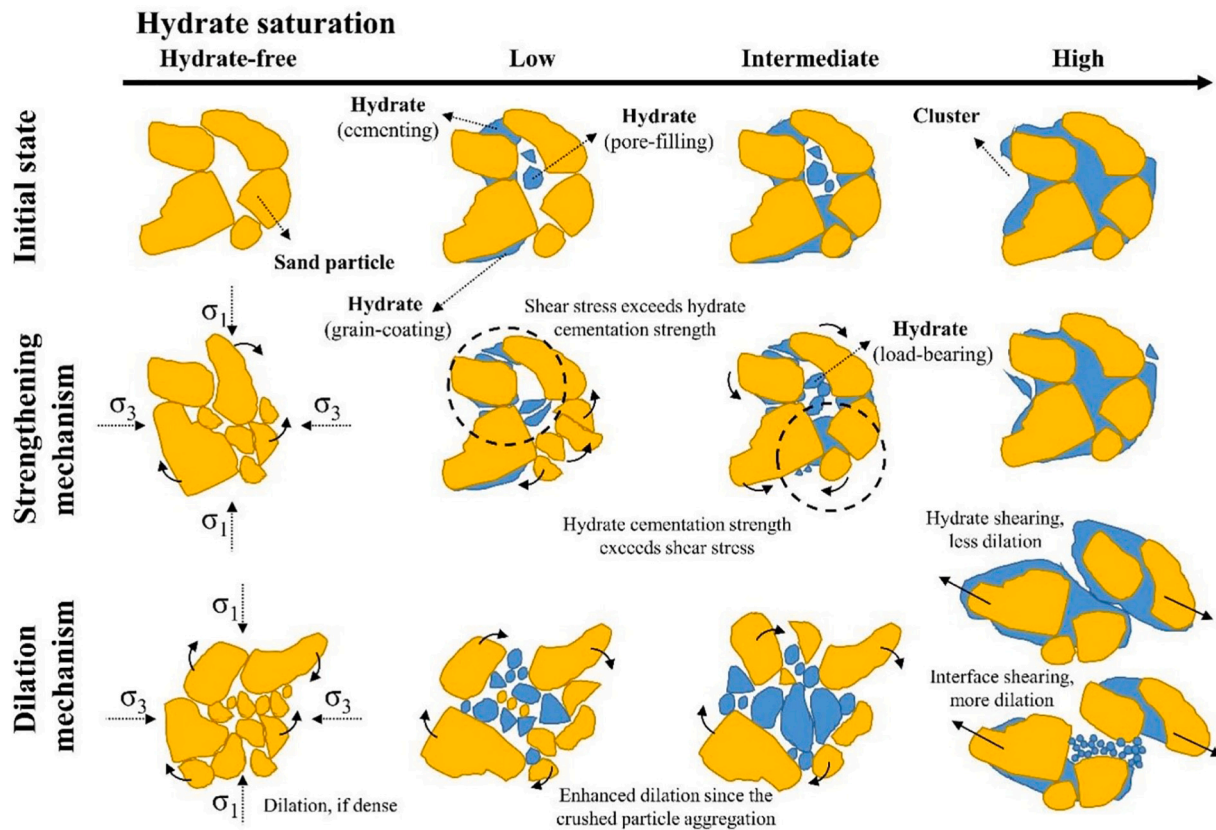
Fig. 8. Pore-scale mechanisms for hydrate-bearing sediments, adapted from (Wu et al., 2020) with permission from the American Chemical Society.

Table 7
Available literature on gas hydrate permeability/seepage using microcomputed tomography.

Reference	Hydrate	Porous media	Aqueous phase	Temperature (K)	Pressure (MPa)	Remarks
(Seol et al., 2006)	Methane	Sand samples 37.8–90 mm	Water	276.65	3	• The saturation of the aqueous phase and hydrate is nonuniform, and the water flows in lower saturation regions
(Seol and Kneafsey, 2008)	Methane	Moist sand pack		277.15	5.5	• Water-flow paths vary in high hydrate saturation and porosity regions
(Konno et al., 2013)	Methane	Cylindrical ($d = 50$ mm; $l = 200$ mm)	Water	273.8	8.1	• Predicted effective permeability depends on hydrate saturation
(Wang et al., 2015a)	Methane	Quartz sand	Water	273.35	5.6	• As hydrate saturation increases, the average pore and throat radii decrease, and permeability decreases
(Wang et al., 2015b)	Methane	Six quartz sand types	Water	273.35	5.6	• The increase in the contact angle corresponds to a decrease in the wettability of porous media containing hydrate, increasing water-phase relative permeability
(Mahabadi et al., 2016a)	Hydrate deposit at the Mallik site in Canada	–	–	–	–	• Hydrate morphology significantly affects gas permeability, and water permeability is slightly affected by hydrate saturation; higher gas and water permeability can be achieved with a heterogeneous surface
(Mahabadi et al., 2016b)	THF hydrate	Micro model	water	–	–	• With increased hydrate saturation, capillary pressure and gas entry pressure also increases
(Wang et al., 2015a)	Methane	Different-sized quartz glass beads	–	–	–	• Large particles tend to have larger absolute permeability and porosity but lower capillary pressure
(Yang et al., 2018)	Methane	Three sand particles: dolomite, quartz, and feldspar	Water	273.65	7.2	• Pore space is greatly affected by the hydrate formation by creating a snap-off effect
(Chen et al., 2018)	Xenon gas	Sand	Brine	296.15 ± 274.15	3.5–3.7	• Gas permeability decreases with the existence of porous hydrate
(Wang et al., 2018b)	Methane	Quartz sand 0.01–1.0 mm	Deionized water	275.15	4	• Hydrate formation and dissociation greatly affect flow properties and pore morphology, and the relative water permeability decreases with increased hydrate saturation
(Wang et al., 2018c)	Methane	Quartz sand	Deionized water	275.15	4	• Absolute permeability variation is significantly affected by pore and throat radii, which are influenced by hydrate growth

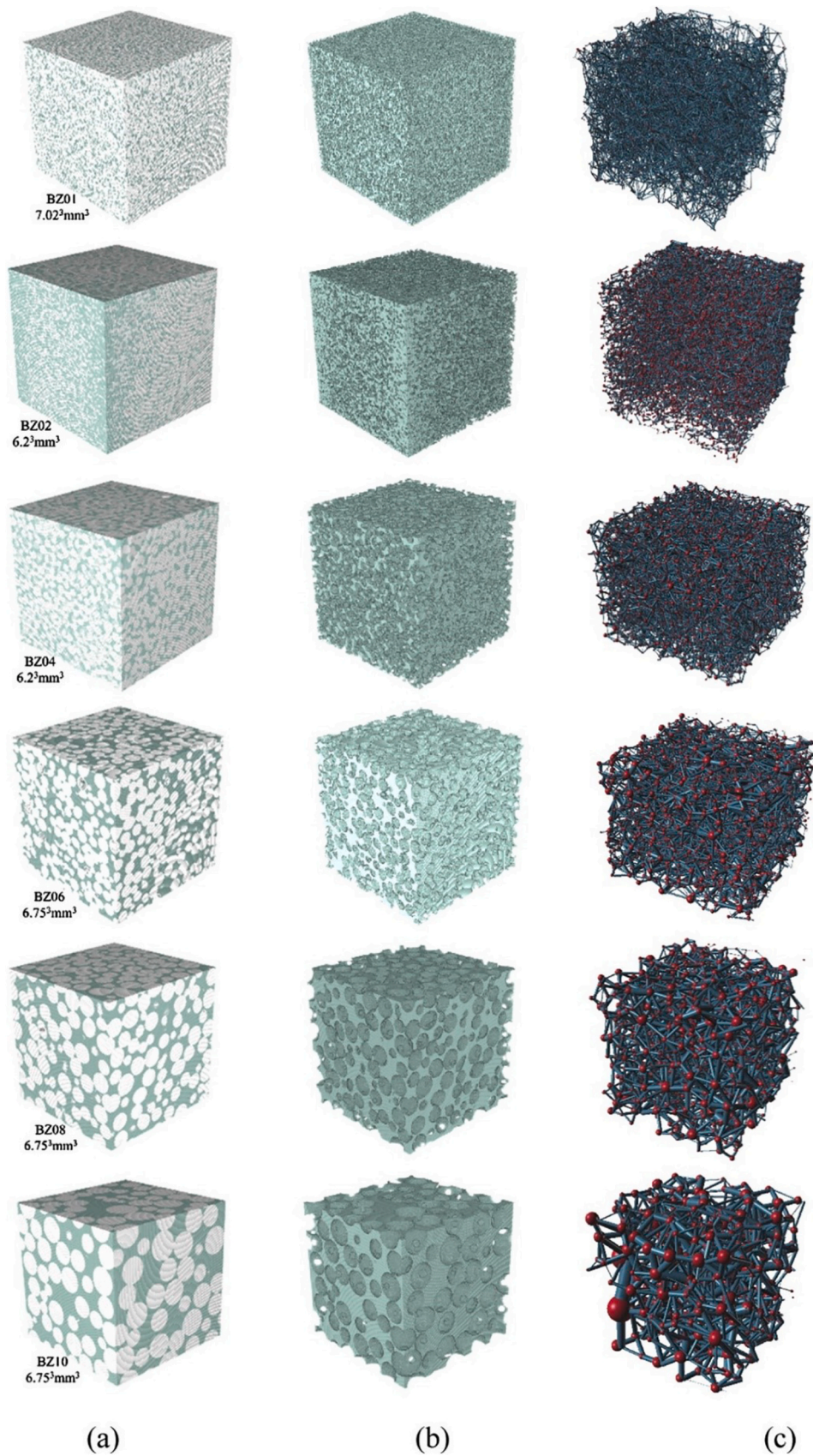*Note:* THF = tetrahydrofuran; d = diameter; l = length.

Fig. 9. Schematic of pore network mode extraction using microcomputed tomography: (a) methane hydrate in porous media, (b) fluid flowing in the pore space, and (c) pore network representation, adapted from (Wang et al., 2016a) with permission from Elsevier.

to determine the high precision of hydrate morphology in the small pores of HBS. Hence, extensive research to address this limitation is needed.

- More complex techniques (e.g., pore network modeling and artificial intelligence deep learning) are required to reproduce μCT images to optimize the restoration of HBS morphology and computational accuracy.
- The implication of numerous parameters on hydrate nucleation behavior and seepage characteristics, such as salinity, grain surface wettability, and pore structure reformation, requires extensive research.
- The presence of organic materials in reservoirs influences wettability. Thus, studies on the influence of wettability on gas hydrate formation and dissociation are crucial. Furthermore, such studies using μCT can provide critical insight into gas hydrate characterization. Hence, it is recommended that researchers investigate gas hydrate wettability using μCT imaging.
- Numerical and molecular dynamic simulation methods can have great potential for NGH characterization because experimental methods may encounter challenges due to the complexity of actual geological conditions. It can also provide a means of validating observations from μCT and other experimental techniques.
- Fossil fuels, such as oil and coal, are depleting rapidly, and reliance is emerging on renewables, such as solar, wind, geothermal, and hydrogen, as new clean energy producers to achieve the global energy demand with no greenhouse gas emissions. Hydrogen is gaining substantial attention among these renewable energy sources as a sustainable substitute. Hydrogen can be produced from nonrenewable and renewable sources and is considered the "fuel of the future." Hence, an innovative approach to hydrogen storage via gas hydrates is recommended.

6. Summary and conclusions

The use of μCT imaging technology to investigate gas hydrate formation and dissociation mechanisms, such as pore behaviors, permeability and seepage properties, and saturation and percolation of HBSs, is critical. The distribution and occurrence patterns of hydrates were directly studied using the μCT experimental technique. In addition, the μCT imaging technique can provide crucial data for developing more precise numerical models to calculate HBS permeability and other seepage parameters. Moreover, μCT scanning is often used to assess the quality and ability of sediments to produce gas hydrates. Therefore, the current study offers a fundamental understanding of the application of μCT to evaluate gas hydrates. Based on the reviewed data, the following conclusions are drawn:

- Three hydrate types are identified: type I (sI), type II (sII), and type H (sH). The occurrence of NGHs depends on the temperature and pressure conditions. Hydrates are thermodynamically stable under low-temperature and high-pressure conditions.
- The initial process of hydrate formation involves arranging the constituent particles into hydrate crystals (hydrate nucleation), promoted by the presence of clay minerals.
- Nucleation of gas hydrates occurs randomly with many parameters, such as saturation, salinity, pore-size distribution, and mineralogy, affecting the nucleation process.
- Estimating gas hydrate physical properties (thermal conductivity, molecular weight, heat capacity, density, and mechanical and electrical properties) is complex because these properties depend upon multiple factors, including (i) hydrate type, (ii) saturation degree, and (iii) the encaged guest molecule in the gas hydrate. Thus, robust characterization techniques and equipment, such as the μCT or recently emerging combined techniques, are needed.

- The advancement in μCT imaging technology is evident from the ten-fold increase in its acquisition speed every five years, indicating the promising potential of its applications.
- Hydrates grow and percolate within porous media. The percolation behavior is affected by several factors, such as permeability, porosity, hydrate saturation, wettability, pore size, and capillarity.
- Different hydrate growth/filling modes include encrustation/coating (laminating), cementing, matrix-supporting, and pore-filling modes.
- The mechanical strength of HBSs is significantly affected by the hydrate morphology, saturation, and wettability.
- Moreover, the stress-strain behavior of HBSs depends on confining pressure, particle size, and hydrate concentration. As the hydrate saturation increases, the friction angle, strength, cohesion, and stiffness of HBSs also increase.
- Last, gas hydrate formation and dissociation greatly affect the flow properties and pore morphology. As hydrate saturation increases, the average pore and throat radii decrease, reducing permeability.

Declaration of Competing Interest

The authors declare that they have no competing financial interests or personal relationships that could have appeared to influence the work reported in this paper.

Data availability

Data will be made available on request.

Acknowledgments

References

Abbasi, G.R., Al-Yaseri, A., Awan, F.U.R., Isah, A., Keshavarz, A., Iglauer, S., 2021. Effect of rock wettability on the electric resistivity of hydrate formations: an experimental investigation. Energy Fuels 35 (24), 20037–20045.

Abbasi, G.R., Al-Yaseri, A., Isah, A., Keshavarz, A., Iglauer, S., 2021b. Influence of rock wettability on THF hydrate saturation and distribution in sandstones. J. Phys. Chem. B 125 (31), 17323–17332.

Aksnes, D., Kimtys, L., 2004. 1H and 2H NMR studies of benzene confined in porous solids: melting point depression and pore size distribution. Solid State Nucl. Magn. Reson. 25 (1–3), 146–152.

Al-Raoush, R., Hannun, J., Jarrar, Z., Alshibli, K., Jung, J., 2019. Impact of fines type on gas flow using 3D micro-computed tomography. In: SPE Kuwait Oil & Gas Show and Conference. OnePetro.

Al-Shajalee, F., Seyyedi, M., Verrall, M., Arif, M., Al-Yaseri, A.Z., Tadé, M.O., Wood, C., Iglauer, S., Saeedi, A., 2022. Impact of prolonged water-gas flow on the performance of polyacrylamide. J. Appl. Polym. Sci. 139 (17), 52037.

Al-Anssari, S., Ali, M., Alajmi, M., et al., 2021. Synergistic effect of nanoparticles and polymers on the rheological properties of injection fluids: implications for enhanced oil recovery. Energy & Fuels 35 (7), 6125–6135.

Ali, M., 2018. Effect of Organic Surface Concentration on CO2-Wettability of Reservoir Rock. Masters Dissertation. Curtin University.

Ali, M., Jha, N.K., Pal, N., et al., 2022. Recent advances in carbon dioxide geological storage, experimental procedures, influencing parameters, and future outlook. Earth-Science Rev. 225, 103895.

Ali, M., Yekeen, N., Pal, N., Keshavarz, A., Iglauer, S., Hoteit, H., 2022. Influence of organic molecules on wetting characteristics of mica/H2/brine systems: implications for hydrogen structural trapping capacities. J. Colloid Interf. Sci. 608, 1739–1749.

Almenningen, S., Iden, E., Fernø, M.A., Ersland, G., 2018. Salinity effects on pore-scale methane gas hydrate dissociation. J. Geophys. Res. Solid Earth 123 (7), 5599–5608.

Arif, M., Abu-Khamsin, S.A., Iglauer, S., 2019. Wettability of rock/CO2/brine and rock/oil/CO2-enriched-brine systems: critical parametric analysis and future outlook. Adv. Colloid Interf. Sci. 268, 91–113.

Arif, M., Mahmoud, M., Zhang, Y., Iglauer, S., 2021. X-ray tomography imaging of shale microstructures: a review in the context of multiscale correlative imaging. Int. J. Coal Geol. 233, 103641.

Bai, Y., Bai, Q., 2018. Subsea engineering handbook. Gulf Professional Publishing.

Biot, M.A., 1955. Theory of elasticity and consolidation for a porous anisotropic solid. J. Appl. Phys. 26 (2), 182–185.

Blunt, M.J., Bijeljic, B., Dong, H., Gharbi, O., Iglauer, S., Mostaghimi, P., Paluszny, A., Pentland, C., 2013. Pore-scale imaging and modelling. Adv. Water Resour. 51, 197–216.

Bu, Q., Meng, Q., Dong, J., Li, C., Liu, C., Zhao, J., Wang, Z., Zhao, W., Kang, J., Hu, G., 2022a. Integration of pore-scale visualization and an ultrasonic test system of methane hydrate-bearing sediments. Energies 15 (14), 4938.

Bu, Q., Xing, T., Li, C., Zhao, J., Liu, C., Wang, Z., Zhao, W., Kang, J., Meng, Q., Hu, G., 2022b. Effect of hydrate microscopic distribution on acoustic characteristics during hydrate dissociation: an insight from combined acoustic-CT detection study. J. Marine Sci. Eng. 10 (8), 1089.

Carroll, J., 2020. Natural gas hydrates: a guide for engineers. Gulf Professional Publishing.

Cha, M., Shin, K., Lee, H., Moudrakovski, I.L., Ripmeester, J.A., Seo, Y., 2015. Kinetics of methane hydrate replacement with carbon dioxide and nitrogen gas mixture using in situ NMR spectroscopy. Environ. Sci. Technol. 49 (3), 1964–1971.

Chao, W., Harteneck, B.D., Liddle, J.A., Anderson, E.H., Attwood, D.T., 2005. Soft X-ray microscopy at a spatial resolution better than 15 nm. Nature 435 (7046), 1210–1213.

Chaouachi, M., Falenty, A., Sell, K., Enzmann, F., Kersten, M., Haberthür, D., Kuhs, W.F., 2015. Microstructural evolution of gas hydrates in sedimentary matrices observed with synchrotron X-ray computed tomographic microscopy. Geochem. Geophys. Geosyst. 16 (6), 1711–1722.

Chen, Q., Liu, C., Wu, N., Li, C., Chen, G., Sun, J., Meng, Q., Bu, Q., Li, Y., 2022. Experimental apparatus for resistivity measurement of gas hydrate-bearing sediment combined with x-ray computed tomography. Rev. Sci. Instrum. 93 (9), 094708.

Chen, Q., Liu, C.L., Ye, Y.G., 2012. Differential scanning calorimetry research of hydrates phase equilibrium in porous media. Adv. Mater. Res. Trans. Tech. Publ. 2122–2126.

Chen, W., Hartman, R.L., 2018. Methane hydrate intrinsic dissociation kinetics measured in a microfluidic system by means of in situ Raman spectroscopy. Energy Fuel 32 (11), 11761–11771.

Chen, X., Verma, R., Espinoza, D.N., Prodanović, M., 2018. Pore-scale determination of gas relative permeability in hydrate-bearing sediments using X-ray computed micro-tomography and lattice Boltzmann method. Water Resour. Res. 54 (1), 600–608.

Chibura, P.E., Zhang, W., Luo, A., Wang, J., 2022. A review on gas hydrate production feasibility for permafrost and marine hydrates. J. Nat. Gas Sci. Eng. 104441.

Chong, Z.R., Yang, S.H.B., Babu, P., Linga, P., Li, X.-S., 2016. Review of natural gas hydrates as an energy resource: prospects and challenges. Appl. Energy 162, 1633–1652.

Chung, S.-Y., Kim, J.-S., Stephan, D., Han, T.-S., 2019. Overview of the use of micro-computed tomography (micro-CT) to investigate the relation between the material characteristics and properties of cement-based materials. Constr. Build. Mater. 229, 116843.

Cnudde, V., Boone, M.N., 2013. High-resolution X-ray computed tomography in geosciences: a review of the current technology and applications. Earth Sci. Rev. 123, 1–17.

Daigle, H., 2016. Relative permeability to water or gas in the presence of hydrates in porous media from critical path analysis. J. Pet. Sci. Eng. 146, 526–535.

Dierolf, M., Menzel, A., Thibault, P., Schneider, P., Kewish, C.M., Wepf, R., Bunk, O., Pfeiffer, F., 2010. Ptychographic X-ray computed tomography at the nanoscale. Nature 467 (7314), 436–439.

Dillon, W.P., 2002. Gas hydrates in the ocean environment..

Dong, H., Sun, J., Arif, M., Golsanami, N., Yan, W., Zhang, Y., 2020. A novel hybrid method for gas hydrate filling modes identification via digital rock. Mar. Pet. Geol. 115, 104255.

Dong, H., Wang, J., Xie, Z., Wang, B., Zhang, L., Shi, Q., 2021a. Potential applications based on the formation and dissociation of gas hydrates. Renew. Sust. Energ. Rev. 143, 110928.

Dong, H., Zhang, Y., Lebedev, M., Arif, M., Yuan, Y., Iglauer, S., 2021b. Simulating coal permeability change as a function of effective stress using a microscale digital rock model. Energy Fuel 35 (10), 8756–8762.

Dong, L., Li, Y., Liu, C., Liao, H., Chen, G., Chen, Q., Liu, L., Hu, G., 2019. Mechanical properties of methane hydrate-bearing interlayered sediments. J. Ocean Univ. China 18 (6), 1344–1350.

Du, J.-W., Liang, D.-Q., Dai, X.-X., Li, D.-L., Li, X.-J., 2011. Hydrate phase equilibrium for the (hydrogen+ tert-butylamine+ water) system. J. Chem. Thermodyn. 43 (4), 617–621.

Fan, S., Liang, D., Guo, K., 2001. Hydrate equilibrium conditions for cyclopentane and a quaternary cyclopentane-rich mixture. J. Chem. Eng. Data 46 (4), 930–932.

Fu, J., Wu, N., Wu, D., Su, Q., 2017. A solid-state 13C NMR and laser Raman spectroscopy study on synthesized methane hydrates. Chin. J. Magn. Reson. 34 (2).

Ghiassian, H., Grozic, J.L., 2013. Strength behavior of methane hydrate bearing sand in undrained triaxial testing. Mar. Pet. Geol. 43, 310–319.

Gilson, D., McDowell, C., 1961. Nuclear magnetic resonance studies of urea and thiourea adducts. Mol. Phys. 4 (2), 125–134.

Godard, P., Carbone, G., Allain, M., Mastropietro, F., Chen, G., Capello, L., Diaz, A., Metzger, T., Stangl, J., Chamard, V., 2011. Three-dimensional high-resolution quantitative microscopy of extended crystals. Nat. Commun. 2 (1), 1–6.

Gupta, A., Moridis, G.J., Kneafsey, T.J., Sloan Jr., E., 2009. Modeling pure methane hydrate dissociation using a numerical simulator from a novel combination of X-ray computed tomography and macroscopic data. Energy Fuel 23 (12), 5958–5965.

Haligva, C., Linga, P., Ripmeester, J.A., Englezos, P., 2010. Recovery of methane from a variable-volume bed of silica sand/hydrate by depressurization. Energy Fuel 24 (5), 2947–2955.

Handa, Y.P., Cook, J.G., 1987. Thermal conductivity of xenon hydrate. J. Phys. Chem. 91 (25), 6327–6328.

Hassanpouryouzband, A., Joonaki, E., Farahani, M.V., Takeya, S., Ruppel, C., Yang, J., English, N.J., Schicks, J.M., Edlmann, K., Mehrabian, H., 2020. Gas hydrates in sustainable chemistry. Chem. Soc. Rev. 49 (15), 5225–5309.

Hosseini, M., Arif, M., Keshavarz, A., Iglauer, S., 2021. Neutron scattering: a subsurface application review. Earth Sci. Rev. 221, 103755.

Hu, G.-W., Li, C.-F., Ye, Y.-G., Liu, C.-L., Zhang, J., Diao, S.-B., 2014. Observation of gas hydrate distribution in sediment pore space. Chin. J. Geophys. 57 (5), 1675–1682.

Hyodo, M., Li, Y., Yoneda, J., Nakata, Y., Yoshimoto, N., Kajiyama, S., Nishimura, A., Song, Y., 2014. A comparative analysis of the mechanical behavior of carbon dioxide and methane hydrate-bearing sediments. Am. Mineral. 99 (1), 178–183.

Hyodo, M., Li, Y., Yoneda, J., Nakata, Y., Yoshimoto, N., Nishimura, A., Song, Y., 2013. Mechanical behavior of gas-saturated methane hydrate-bearing sediments. Journal of geophysical research: solid earth 118 (10), 5185–5194.

Iglauer, S., Akhondzadeh, H., Abid, H., et al., 2022. Hydrogen flooding of a coal core: effect on coal swelling. Geophys. Res. Lett. 49 (6), e2021GL096873.

Isah, A., Arif, M., Hassan, A., Mahmoud, M., Iglauer, S., 2022. Fluid–rock interactions and its implications on EOR: critical analysis, experimental techniques and knowledge gaps. Energy Rep. 8, 6355–6395.

Jiang, J., WU, Q., PU, Y., XING, L., 2005. Computerized tomography identifying and its imaging characteristics incombination and dissociation process of methane hydrate [J]. Nat. Gas Geosci. 6.

Jin, Y., Konno, Y., Nagao, J., 2014. Pressurized subsampling system for pressured gas-hydrate-bearing sediment: Microscale imaging using X-ray computed tomography. Rev. Sci. Instrum. 85 (9), 094502.

Kajiyama, S., Wu, Y., Hyodo, M., Nakata, Y., Nakashima, K., Yoshimoto, N., 2017. Experimental investigation on the mechanical properties of methane hydrate-bearing sand formed with rounded particles. J. Nat. Gas Sci. Eng. 45, 96–107.

Ketcham, R.A., 2005. Computational methods for quantitative analysis of three-dimensional features in geological specimens. Geosphere 1 (1), 32–41.

Ketcham, R.A., Carlson, W.D., 2001. Acquisition, optimization and interpretation of X-ray computed tomographic imagery: applications to the geosciences. Comput. Geosci. 27 (4), 381–400.

Kneafsey, T.J., Seol, Y., Gupta, A., Tomutsa, L., 2010. Permeability of laboratory-formed methane-hydrate-bearing sand: measurements and observations using X-ray computed tomography.

Konno, Y., Jin, Y., Uchiumi, T., Nagao, J., 2013. Multiple-pressure-tapped core holder combined with X-ray computed tomography scanning for gas–water permeability measurements of methane-hydrate-bearing sediments. Rev. Sci. Instrum. 84 (6), 064501.

Lei, L., Liu, Z., Seol, Y., Boswell, R., Dai, S., 2019. An investigation of hydrate formation in unsaturated sediments using X-ray computed tomography. J. Geophys. Res. Solid Earth 124 (4), 3335–3349.

Lei, L., Santamarina, J., 2018. Laboratory strategies for hydrate formation in fine-grained sediments. J. Geophys. Res. Solid Earth 123 (4), 2583–2596.

Lei, L., Seol, Y., 2020. Pore-Scale Investigation of methane Hydrate-Bearing Sediments under Triaxial Condition. Geophys. Res. Lett. 47 (5) e2019GL086448.

Li, C., Hu, G., Ye, Y.-G., Liu, C., Cheng, J., Zhang, L.-K., Zheng, R.-E., 2013. Microscopic distribution of gas hydrate in sediment determined by X-ray computerized tomography. J. Optoelectron. Laser 24, 551–557.

Li, G., Wu, D.-M., Li, X.-S., Lv, Q.-N., Li, C., Zhang, Y., 2017a. Experimental measurement and mathematical model of permeability with methane hydrate in quartz sands. Appl. Energy 202, 282–292.

Li, L., Huang, B., Tan, Y., Deng, X., Li, Y., Zheng, H., 2017b. Geometric heterogeneity of continental shale in the Yanchang Formation, Southern Ordos Basin, China. Sci. Reports 7 (1), 1–12.

Li, S., Liu, L., Chai, P., Li, X., He, J., Zhang, Z., Wei, L., 2019a. Imaging hydraulic fractures of shale cores using combined positron emission tomography and computed tomography (PET-CT) imaging technique. J. Pet. Sci. Eng. 182, 106283.

Li, Y., Wu, P., Liu, W., Sun, X., Cui, Z., Song, Y., 2019b. A microfocus x-ray computed tomography based gas hydrate triaxial testing apparatus. Rev. Sci. Instrum. 90 (5), 055106.

Liang, D., Guo, K., Wang, R., Fan, S., 2001. Hydrate equilibrium data of 1, 1, 1, 2-tet-rafluoroethane (HFC-134a), 1, 1-dichloro-1-fluoroethane (HCFC-141b) and 1, 1-difluoroethane (HFC-152a). Fluid Phase Equilib. 187, 61–70.

Libbrecht, K.G., Lui, K., 2004. An investigation of laboratory-grown ice spikes. J. Glaciol. 50 (170), 371–374.

Lindquist, W.B., Venkatarangan, A., Dunsmuir, J., Wong, T.F., 2000. Pore and throat size distributions measured from synchrotron X-ray tomographic images of Fontainebleau sandstones. J. Geophys. Res. Solid Earth 105 (B9), 21509–21527.

Litao, C., Changyu, S., Guangjin, C., Yunqiang, N., Zhansong, S., Yantao, L., 2009. Measurements of hydrate equilibrium conditions for CH4, CO2, and CH4+ C2H6+ C3H8 in various systems by step-heating method. Chin. J. Chem. Eng. 17 (4), 635–641.

Liu, C., Meng, Q., He, X., Li, C., Ye, Y., Zhang, G., Liang, J., 2015. Characterization of natural gas hydrate recovered from Pearl River Mouth basin in South China Sea. Mar. Pet. Geol. 61, 14–21.

Liu, C., Meng, Q., Hu, G., Li, C., Sun, J., He, X., Wu, N., Yang, S., Liang, J., 2017. Characterization of hydrate-bearing sediments recovered from the Shenhu area of the South China Sea. Interpretation 5 (3), SM13-SM23.

Liu, C., Ye, Y., Meng, Q., He, X., Lu, H., Zhang, J., Liu, J., Yang, S., 2012. The characteristics of gas hydrates recovered from Shenhu Area in the South China Sea. Mar. Geol. 307, 22–27.

Liu, C., Ye, Y., Meng, Q., Lu, Z., Zhu, Y., Liu, J., Yang, S., 2010. Raman spectroscopic characteristics of natural gas hydrate recovered from Shenhu area in South China Sea and Qilian Mountain permafrost.

Liu, L., Ryu, B., Sun, Z., Wu, N., Cao, H., Geng, W., Zhang, X., Jia, Y., Xu, C., Guo, L., 2019. Monitoring and research on environmental impacts related to marine natural gas hydrates: review and future perspective. J. Nat. Gas Sci. Eng. 65, 82–107.

Liu, X., Dong, H., Yan, W., Arif, M., Zhang, Y., Golsanami, N., 2021a. Influence of gas hydrate saturation and pore habits on gas relative permeability in gas hydrate-bearing sediments: Theory, experiment and case study. J. Nat. Gas Sci. Eng. 95, 104171.

Liu, Y., Song, Y., Chen, Y., Yao, L., Li, Q., 2010b. The detection of tetrahydrofuran hydrate formation and saturation using magnetic resonance imaging technique. J. Nat. Gas Sci. Eng. 19 (3), 224–228.

Liu, Y., Xie, D., Zhou, R., Zhang, Y., 2021b. 3D X-ray micro-computed tomography imaging for the microarchitecture evaluation of porous metallic implants and scaffolds. Micron 142, 102994.

Lv, J., Zhao, J., Jiang, L., Liu, Y., Mu, H., 2020. A review of micro computed tomography studies on the gas hydrate pore habits and seepage properties in hydrate bearing sediments. J. Nat. Gas Sci. Eng. 103555.

Ma, Q.-L., Chen, G.-J., Ma, C.-F., Zhang, L.-W., 2008. Study of vapor–hydrate two-phase equilibria. Fluid Phase Equilib. 265 (1–2), 84–93.

Mahabadi, N., Dai, S., Seol, Y., Sup Yun, T., Jang, J., 2016a. The water retention curve and relative permeability for gas production from hydrate-bearing sediments: Pore-network model simulation. Geochem. Geophys. Geosyst. 17 (8), 3099–3110.

Mahabadi, N., Zheng, X., Jang, J., 2016b. The effect of hydrate saturation on water retention curves in hydrate-bearing sediments. Geophys. Res. Lett. 43 (9), 4279–4287.

Mahesar, A.A., Ali, M., Shar, A.M., Memon, K.R., Mohanty, U.S., et al., 2020. Effect of cryogenic liquid nitrogen on the morphological and petrophysical characteristics of tight gas sandstone rocks from kirthar fold belt, Indus Basin, Pakistan. Energy & Fuels 34 (11), 14548–14559.

Maire, E., Withers, P.J., 2014. Quantitative X-ray tomography. Int. Mater. Reviews 59 (1), 1–43.

Malagar, B.R., Lijith, K., Singh, D., 2019. Formation & dissociation of methane gas hydrates in sediments: a critical review. J. Nat. Gas Sci. Eng. 65, 168–184.

Maser, J., 2001. In: Soft X-rays and Extreme Ultraviolet Radiation: Principles and Applications. David Attwood. 1999. Cambridge University Press, Cambridge, UK, p. 470 pages.(hardback, $59.95). Microscopy and Microanalysis, 7(6): 536-536.

Masui, A., Haneda, H., Ogata, Y., Aoki, K., 2005. Effects of methane hydrate formation on shear strength of synthetic methane hydrate sediments. In: The Fifteenth International Offshore and Polar Engineering Conference. OnePetro.

Mathews, J.P., Campbell, Q.P., Xu, H., Halleck, P., 2017. A review of the application of X-ray computed tomography to the study of coal. Fuel 209, 10–24.

Mees, F., Swennen, R., Van Geet, M., Jacobs, P., 2003. Applications of X-ray computed tomography in the geosciences. Geol. Soc. Lond., Spec. Publ. 215 (1), 1–6.

Melnikov, V., Nesterov, A., Podenko, L., Reshetnikov, A., Shalamov, V., 2012. NMR evidence of supercooled water formation during gas hydrate dissociation below the melting point of ice. Chem. Eng. Sci. 71, 573–577.

Meng, Q.-G., LIU, C.-L., HE, X.-L., YE, Y.-G., ZHU, Y.-H., XIA, N., 2011. Laser-Raman spectroscopy characteristics of natural gas hydrates from Qilian Mountain permafrost. Geol. Bull. China 30 (12), 1863–1867.

Meng, Q.-G., Liu, C.-L., Ye, Y.-G., 2011b. (13) C solid-state nuclear magnetic resonance investigations of gas hydrate structures. Fenxi Huaxue 39 (9), 1447–1450.

Meng, Q., Liu, C., Li, C., He, X., Wang, F., Lu, Z., Wen, H., Li, Y., Wang, W., 2015a. Raman spectroscopic characteristics of natural gas hydrates from Juhugeng drilling area. Qinghai. Geoscience 29 (5), 1180–1188.

Meng, Q., Liu, C., Ye, Y., Li, C., 2015b. Measurement of micro-structure features of binary CH4-THF clathrate hydrate based on the 13C solid state NMR. Nat. Gas Ind. 35 (3), 135–140.

Miura, H., Takata, M., Tajima, D., Tsuyuki, K., 2006. Promotion of methane hydrate dissociation by underwater ultrasonic wave. Jpn. J. Appl. Phys. 45 (5S), 4816.

Miyazaki, K., Masui, A., Sakamoto, Y., Aoki, K., Tenma, N., Yamaguchi, T., 2011. Triaxial compressive properties of artificial methane-hydrate-bearing sediment. J. Geophys. Res. Solid Earth 116 (B6).

Miyazaki, K., Oikawa, Y., Haneda, H., Yamaguchi, T., 2016. Triaxial compressive property of artificial CO2-hydrate sand. Int. J. Offshore Polar Eng. 26 (03), 315–320.

Otsu, N., 1979. A threshold selection method from gray-level histograms. IEEE Trans. Syst. Man Cybernet. 9 (1), 62–66.

Pal, N., Zhang, X., Ali, M., Mandal, A., Hoteit, H., 2022. Carbon dioxide thickening: a review of technological aspects, advances and challenges for oilfield application. Fuel, 122947.

Pu, Y.-B., Wu, Q.-B., Jiang, G.-L., 2007. CT experiment and analyses of methane hydrate in porous media in closed system. Adv. Earth Sci. 22 (4), 362–368.

Qingguo, M., Changling, L., Yuguang, Y., 2012. In situ monitoring ice melting and tetrahydrofuran hydrates dissociation with magnetic resonance imaging. J. Basic Sci. Eng. 20 (1), 11–20.

Rees, E.V., Kneafsey, T.J., Seol, Y., 2011. Methane hydrate distribution from prolonged and repeated formation in natural and compacted sand samples: X-ray CT observations. J. Geol. Res. 2011 (791815), 2011.

Ripmeester, J.A., 2000. Hydrate research-from correlations to a knowledge-based discipline: the importance of structure. Ann. N. Y. Acad. Sci. 912 (1), 1–16.

Ripmeester, J.A., John, S.T., Ratcliffe, C.I., Powell, B.M., 1987. A new clathrate hydrate structure. Nature 325 (6100), 135–136.

Ruan, X., Li, X.-S., Xu, C.-G., 2021. A review of numerical research on gas production from natural gas hydrates in China. J. Nat. Gas Sci. Eng. 85, 103713.

Sadeq, D., Iglauer, S., Lebedev, M., Rahman, T., Zhang, Y., Barifcani, A., 2018. Experimental pore-scale analysis of carbon dioxide hydrate in sandstone via X-Ray micro-computed tomography. Int. J. Greenh. Gas Contr. 79, 73–82.

Sasaki, S., Hori, S., Kume, T., Shimizu, H., 2003. Microscopic observation and in situ Raman scattering studies on high-pressure phase transformations of a synthetic nitrogen hydrate. J. Chem. Phys. 118 (17), 7892–7897.

Saxena, N., Hofmann, R., Alpak, F.O., Dietderich, J., Hunter, S., Day-Stirrat, R.J., 2017. Effect of image segmentation & voxel size on micro-CT computed effective transport & elastic properties. Mar. Pet. Geol. 86, 972–990.

Schindelin, J., Arganda-Carreras, I., Frise, E., Kaynig, V., Longair, M., Pietzsch, T., Preibisch, S., Rueden, C., Saalfeld, S., Schmid, B., 2012. Fiji: an open-source platform for biological-image analysis. Nat. Methods 9 (7), 676–682.

Schindler, M., Batzle, M.L., Prasad, M., 2017. Micro X-Ray computed tomography imaging and ultrasonic velocity measurements in tetrahydrofuran-hydrate-bearing sediments. Geophys. Prospect. 65 (4), 1025–1036.

Schindler, M., Kneafsey, T., Nakagawa, S., 2015. N2/CO2 substitution in methane-hydrate bearing sediments, 3rd International Workshop on Rock Physics, 13th–17th April..

Seol, Y., Kneafsey, T.J., 2008. Fluid flow through heterogeneous methane hydrate-bearing sand: observations using x-ray CT scanning. In: Proceedings of the 6th International Conference on Gas Hydrates (ICGH 2008), pp. 6–10.

Seol, Y., Kneafsey, T.J., 2009. X-ray computed-tomography observations of water flow through anisotropic methane hydrate-bearing sand. J. Pet. Sci. Eng. 66 (3–4), 121–132.

Seol, Y., Kneafsey, T.J., 2011. Methane hydrate induced permeability modification for multiphase flow in unsaturated porous media. J. Geophys. Res. Solid Earth 116 (B8).

Seol, Y., Kneafsey, T.J., Tomutsa, L., Moridis, G.J., 2006. Preliminary relative permeability estimates of methane hydrate-bearing sand.

Shicai, S., Linlin, G., Zhendong, Y., Haifei, L., Yanmin, L., 2022. Thermophysical properties of natural gas hydrates: a reviews. Natural Gas Industry B.

Silin, D.B., Jin, G., Patzek, T.W., 2003. Robust determination of the pore space morphology in sedimentary rocks. In: SPE Annual Technical Conference and Exhibition. OnePetro.

Sloan, E.D., 1998. Gas hydrates: review of physical/chemical properties. Energy Fuel 12 (2), 191–196.

Sloan Jr., E.D., Koh, C.A., Koh, C., 2007. Clathrate hydrates of natural gases. CRC Press.

Strobel, T.A., Hester, K.C., Koh, C.A., Sum, A.K., Sloan Jr., E.D., 2009. Properties of the clathrates of hydrogen and developments in their applicability for hydrogen storage. Chem. Phys. Lett. 478 (4–6), 97–109.

Sum, A.K., Burruss, R.C., Sloan, E.D., 1997. Measurement of clathrate hydrates via Raman spectroscopy. J. Phys. Chem. B 101 (38), 7371–7377.

Sun, C.-Y., Chen, G.-J., Zhang, L.-W., 2010. Hydrate phase equilibrium and structure for (methane+ ethane+ tetrahydrofuran+ water) system. J. Chem. Thermodyn. 42 (9), 1173–1179.

Sun, J., Dong, H., Arif, M., Yu, L., Zhang, Y., Golsanami, N., Yan, W., 2021. Influence of pore structural properties on gas hydrate saturation and permeability: a coupled pore-scale modelling and X-ray computed tomography method. J. Nat. Gas Sci. Eng. 88, 103805.

Sun, Z.-G., Fan, S.-S., Guo, K.-H., Shi, L., Guo, Y.-K., Wang, R.-Z., 2002a. Gas hydrate phase equilibrium data of cyclohexane and cyclopentane. J. Chem. Eng. Data 47 (2), 313–315.

Sun, Z.-G., Fan, S.-S., Guo, K.-H., Shi, L., Wang, R.-Z., 2002b. Equilibrium hydrate formation conditions for methylcyclohexane with methane and a ternary gas mixture. Fluid Phase Equilib. 198 (2), 293–298.

Sun, Z.-G., Fan, S.-S., Shi, L., Guo, Y.-K., Guo, K.-H., 2001. Equilibrium conditions hydrate dissociation for a ternary mixture of methane, ethane, and propane in aqueous solutions of ethylene glycol and electrolytes. J. Chem. Eng. Data 46 (4), 927–929.

Swinkels, W.J., Drenth, R.J., 2000. Thermal reservoir simulation model of production from naturally occurring gas hydrate accumulations. SPE Reserv. Eval. Eng. 3 (06), 559–566.

Ta, X.H., Yun, T.S., Muhunthan, B., Kwon, T.H., 2015. Observations of pore-scale growth patterns of carbon dioxide hydrate using X-ray computed microtomography. Geochem. Geophys. Geosyst. 16 (3), 912–924.

Tariq, M., Soromenho, M.R., Rebelo, L.P.N., Esperança, J.M., 2022. Insights into CO2 hydrates formation and dissociation at isochoric conditions using a rocking cell apparatus. Chem. Eng. Sci. 249, 117319.

Uchida, T., Takagi, A., Kawabata, J., Mae, S., Hondoh, T., 1995. Raman spectroscopic analyses of the growth process of CO2 hydrates. Energy Convers. Manag. 36 (6–9), 547–550.

Van Geet, M., Swennen, R., Wevers, M., 2000. Quantitative analysis of reservoir rocks by microfocus X-ray computerised tomography. Sediment. Geol. 132 (1–2), 25–36.

Wang, B., Dong, H., Liu, Y., Lv, X., Liu, Y., Zhao, J., Song, Y., 2018a. Evaluation of thermal stimulation on gas production from depressurized methane hydrate deposits☆. Appl. Energy 227, 710–718.

Wang, D., Wang, C., Li, C., Liu, C., Lu, H., Wu, N., Hu, G., Liu, L., Meng, Q., 2018b. Effect of gas hydrate formation and decomposition on flow properties of fine-grained quartz sand sediments using X-ray CT based pore network model simulation. Fuel 226, 516–526.

Wang, J.-Q., Zhao, J.-F., Yang, M.-J., Li, Y.-H., Liu, W.-G., Song, Y.-C., 2015a. Permeability of laboratory-formed porous media containing methane hydrate: observations using X-ray computed tomography and simulations with pore network models. Fuel 145, 170–179.

Wang, J., Zhang, L., Zhao, J., Ai, L., Yang, L., 2018c. Variations in permeability along with interfacial tension in hydrate-bearing porous media. J. Nat. Gas Sci. Eng. 51, 141–146.

Wang, J., Zhao, J., Zhang, Y., Wang, D., Li, Y., Song, Y., 2015b. Analysis of the influence of wettability on permeability in hydrate-bearing porous media using pore network models combined with computed tomography. J. Nat. Gas Sci. Eng. 26, 1372–1379.

Wang, J., Zhao, J., Zhang, Y., Wang, D., Li, Y., Song, Y., 2016a. Analysis of the effect of particle size on permeability in hydrate-bearing porous media using pore network models combined with CT. Fuel 163, 34–40.

Wang, L., Fu, Y., Li, J., Sima, L., Wu, Q., Jin, W., Wang, T., 2016b. Mineral and pore structure characteristics of gas shale in Longmaxi formation: a case study of Jiaoshiba gas field in the southern Sichuan Basin China. Arab. J. Geosci. 9 (19), 733.

Wang, L., Gu, L.-J., Lu, H.-L., 2020. Sediment permeability change on natural gas hydrate dissociation induced by depressurization. China Geol. 3 (2), 221–229.

Wang, L., Li, Y., Shen, S., Liu, W., Sun, X., Liu, Y., Zhao, J., 2019. Mechanical behaviours of gas-hydrate-bearing clayey sediments of the South China Sea. Environ. Geotech. 40 (XXXX), 1–13.

Winters, W.J., Waite, W.F., Mason, D., Gilbert, L., Pecher, I., 2007. Methane gas hydrate effect on sediment acoustic and strength properties. J. Pet. Sci. Eng. 56 (1–3), 127–135.

Wu, N.-Y., Liu, C.-L., Hao, X.-L., 2018. Experimental simulations and methods for natural gas hydrate analysis in China. China Geol. 1 (1), 61–71.

Wu, P., Li, Y., Sun, X., Liu, W., Song, Y., 2020. Mechanical characteristics of hydrate-bearing sediment: a review. Energy Fuel 35 (2), 1041–1057.

Wu, Q.-B., Pu, Y.-B., Jiang, G.-L., Deng, Y.-S., Xing, L.-L., Feng, X.-T., 2006. Experimental research of formation and decomposition processes of methane hydrate by computerized tomography. J. Glaciol. Geocryol. 1.

Xie, Y., Li, R., Wang, X.-H., Zheng, T., Cui, J.-L., Yuan, Q., Qin, H.-B., Sun, C.-Y., Chen, G.-J., 2020. Review on the accumulation behavior of natural gas hydrates in porous sediments. J. Nat. Gas Sci. Eng. 83, 103520.

Yan, C., Ren, X., Cheng, Y., Song, B., Li, Y., Tian, W., 2020. Geomechanical issues in the exploitation of natural gas hydrate. Gondwana Res. 81, 403–422.

Yang, L., Ai, L., Xue, K., Ling, Z., Li, Y., 2018. Analyzing the effects of inhomogeneity on the permeability of porous media containing methane hydrates through pore network models combined with CT observation. Energy 163, 27–37.

Yang, L., Falenty, A., Chaouachi, M., Haberthür, D., Kuhs, W.F., 2016a. Synchrotron X-ray computed microtomography study on gas hydrate decomposition in a sedimentary matrix. Geochem. Geophys. Geosyst. 17 (9), 3717–3732.

Yang, L., Zhao, J., Liu, W., Li, Y., Yang, M., Song, Y., 2015. Microstructure observations of natural gas hydrate occurrence in porous media using microfocus X-ray computed tomography. Energy Fuel 29 (8), 4835–4841.

Yang, M., Fu, Z., Zhao, Y., Jiang, L., Zhao, J., Song, Y., 2016b. Effect of depressurization pressure on methane recovery from hydrate–gas–water bearing sediments. Fuel 166, 419–426.

Yang, M., Jing, W., Zhao, J., Ling, Z., Song, Y., 2016c. Promotion of hydrate-based CO2 capture from flue gas by additive mixtures (THF (tetrahydrofuran)+ TBAB (tetra-n-butyl ammonium bromide)). Energy 106, 546–553.

Yao, L., 2010. Study on the Nuclear Magnetic Resonance Imaging of Hydrate in Porous Media. Dalian University of Technology.. M. Sc. dissertation.

Yin, Z., Chong, Z.R., Tan, H.K., Linga, P., 2016. Review of gas hydrate dissociation kinetic models for energy recovery. J.Nat. Gas Sci.Eng. 35, 1362–1387.

Yoneda, J., Jin, Y., Katagiri, J., Tenma, N., 2016. Strengthening mechanism of cemented hydrate-bearing sand at microscales. Geophys. Res. Lett. 43 (14), 7442–7450.

Yun, T.S., Santamarina, J.C., Ruppel, C., 2007. Mechanical properties of sand, silt, and clay containing tetrahydrofuran hydrate. J. Geophys. Res. Solid Earth 112 (B4).

Zhang, W., Li, C., Liu, C., 2016. Identification technology of the CT images for distinguishing the boundary condition of methane hydrate in porous media. Comput. Tomogr. Theory Appl. 25, 13–22.

Zhang, X., Du, Z., Luan, Z., Wang, X., Xi, S., Wang, B., Li, L., Lian, C., Yan, J., 2017. In situ Raman detection of gas hydrates exposed on the seafloor of the South China Sea. Geochem. Geophys. Geosyst. 18 (10), 3700–3713.

Zhang, Y., Bhattacharjee, G., Kumar, R., Linga, P., 2021a. Solidified Hydrogen Storage (Solid-HyStore) via Clathrate Hydrates. Chem. Eng. J. 133702.

Zhang, Y., Zhang, Z., Arif, M., Lebedev, M., Busch, A., Sarmadivaleh, M., Iglauer, S., 2020. Carbonate rock mechanical response to CO2 flooding evaluated by a combined X-ray computed tomography–DEM method. J. Nat. Gas Sci. Eng. 84, 103675.

Zhang, Z., Liu, L., Li, C., Liu, C., Ning, F., Liu, Z., Meng, Q., 2021b. A testing assembly for combination measurements on gas hydrate-bearing sediments using x-ray computed tomography and low-field nuclear magnetic resonance. Rev. Sci. Instrum. 92 (8), 085108.

Zhao, J., Liu, C., Li, C., Zhang, Y., Bu, Q., Wu, N., Liu, Y., Chen, Q., 2022. Pore-scale investigation of the electrical property and saturation exponent of Archie's law in hydrate-bearing sediments. J. Marine Sci. Eng. 10 (1), 111.

Zhao, J., Yang, L., Liu, Y., Song, Y., 2015. Microstructural characteristics of natural gas hydrates hosted in various sand sediments. Phys. Chem. Chem. Phys. 17 (35), 22632–22641.

Zhao, J., Yang, L., Xue, K., Lam, W., Li, Y., Song, Y., 2014. In situ observation of gas hydrates growth hosted in porous media. Chem. Phys. Lett. 612, 124–128.

Zhao, Y., Zhao, J., Shi, D., Feng, Z., Liang, W., Yang, D., 2016. Micro-CT analysis of structural characteristics of natural gas hydrate in porous media during decomposition. J. Nat. Gas Sci. Eng. 31, 139–148.

Zhu, Y., Wang, P., Pang, S., Zhang, S., Xiao, R., 2021. A review of the resource and test production of natural gas hydrates in China. Energy Fuel 35 (11), 9137–9150.